Doctoral Thesis

공학박사학위논문

Lateral p-i-n Diode for Silicon Solar Cell

실리콘 태양전지를 위한 측면 p-i-n 다이오드

February 2017

서울대학교 대학원

Graduate School of Seoul National University

Department of Materials Science and Engineering

Zohreh Kiaee

Lateral p-i-n Diode for Silicon Solar Cell

A dissertation submitted to

Seoul National University

for the degree of Doctor of Philosophy

By

Zohreh Kiaee

Dissertation Advisor: Professor Seung Ki Joo

Department of Materials Science and Engineering

The Graduate School

Seoul National University

February 2017

Abstract

Lateral p-i-n Diode for Silicon Solar Cell

Zohreh Kiaee

Department of Materials Science and Engineering

The Graduate School

Seoul National University

In this thesis, lateral p-i-n diode for silicon solar cell application were studied. The focus was put on the characterization of the lateral structure of p-i-n diode for thin-film silicon solar cells, for the first time. The structure exploits direct light irradiation on the absorber layer, has one-side contact, and can benefit from wide intrinsic region. The efficiency parameters were calculated by considering the effect of different carrier lifetimes and recombination, as a function of intrinsic layer width, as well as the distance between p/i or n/i junctions to contacts, by simulation. From the results, optimum intrinsic region width was defined regarding carrier's lifetime of the cell. Obtained results showed that the distance between p/i or n/i junction to contacts should be kept below 1 μm in order to prevent efficiency reduction. Moreover, in the simulation chapter, the effect of surface recombination on the performance of the lateral cell was evaluated by considering relatively low and relatively high surface recombination velocities (SRV). The simulation results showed that by increasing SRV from 100 cm/s to 1000 cm/s, the open-circuit voltage reduces about 19%. Thus, the requirements on the front surface passivation of the lateral cell type are very high, more than in conventional vertical type cells. Excellent parameter values were

achieved from the simulation results. 706.52 mV open-circuit voltage, 24.16 mA/Cm^2 short-circuit current, 82.66% fill factor, and 14.11% efficiency were obtained from a lateral cell (thickness = 3 μm; intrinsic layer width = 53 μm). At the same time, performance of two configurations of lateral solar cells was investigated by experimental work. Lateral cells were successfully fabricated using polycrystalline-silicon (poly-Si) thin-film prepared by Ni silicide-induced crystallization (SIC) for the first time. I-V characteristics of two types of lateral cells, with isolated (p-i-n) cells and connected (p-i-n) cells were compared in dark and under illumination condition. The configuration with isolated cells showed clear rectifying behavior for a wider range of intrinsic region width compared to the connected cells. At the same values of intrinsic region width, a higher short-circuit current was obtained from isolated cells than the connected cells. The short-circuit current of 3.3 mA/cm^2 and an open-circuit voltage of 0.13 V were obtained from a 400-nm-thick isolated cells. Regarding simulation results and the fact that no optimization was performed in the experimental work, it is expected to obtain higher efficiencies from fabrication, by means of optimizations such as surface texturing, light trapping, anti-reflection coating, and rear reflector. Findings of this work confirmed that the laterally structured p-i-n cell can be a potentially powerful means for producing highly efficient, silicon solar cell. However, in the cost of more complicated fabrication process and maybe higher cost.

Keywords: solar cell, p-i-n diode, lateral solar sell, poly-silicon, Ni silicide-induced crystallization, simulation

Student Number: 2014-30857

Contents

LIST OF TABLES

LIST OF FIGURES

Chapter 1. Introduction

1.1 Thesis Motivation

1.1.1 World Energy Challenge

Today, the most used form of energy is fossil energy. However, fossil energy resources are very limited and produce harmful emissions. Hence, two major problems of mankind are to mitigate climate change that is caused by the emission of the greenhouse gases, and find an alternative sustainable energy resource. Thus, one of the greatest challenges for the human is to transit from the fossil energy sources to the clean and renewable energy sources.

As of 2015, the world population was 7.3 billion and consumed about 30 Terawatts power. By 2050, the population is projected to be over 10 billion and 60 Terawatts power will be consumed [1.1].

1.1.2 Solar Energy and Solar Cell

Among all renewable energy sources, solar cells are the only technology that can satisfy future demand for the sustainable environmentally friendly energy. Solar energy is an abundant and widely available source of energy. Our planet receives enough energy from the Sun to cover the present global annual energy consumption in just one hour. The Earth receives incoming solar radiation with the total energy of approximately 3,850,000 EJ (EJ i.e. exajoules, 1 EJ = 10^{18}) from the Sun per year [1.2]. (see Table 1.1 below and Figure 1.1)

Table. 1.1 Annually solar energy, wind, biomass and human energy consumption.

Annually Solar energy, Wind, Biomass and Human Energy Consumption	
Solar	3,850,000 EJ [1.2]
Wind	2,250 EJ [1.3]
Biomass	3,000 EJ [1.4]
Primary energy use (2015)	487 EJ [1.5]
Electricity (2015)	56.7 [1.6]

A solar cell does not produce any noise or emissions during its operation and is safe. Solar cell technology seems to be the best solution to reduce carbon dioxide and other greenhouse gas emissions into the atmosphere. The Sun light can be directly converted into electricity by the photovoltaic devices or solar cells. Thus, solar cell technology is a promising technology to satisfy the future need for the sustainable environmentally friendly energy [1.7]. The Lewis research group at California Institute of Technology after a systematic analysis of all currently available renewable power (including solar, wind, geothermal, and biomass, etc.) reported that solar energy is the only form of energy abundant enough to meet the world's energy requirements in the next half century [1.8]. Therefore, the lateral p-i-n solar cell research of this work fits in the global theme of "renewable energy". To be specific, it is

aimed in this work to develop, characterize and fabricate a laterally structured p-i-n Si solar cell, which theoretically has potential of having higher efficiencies compared to the conventional vertical p-i-n Si solar cells.

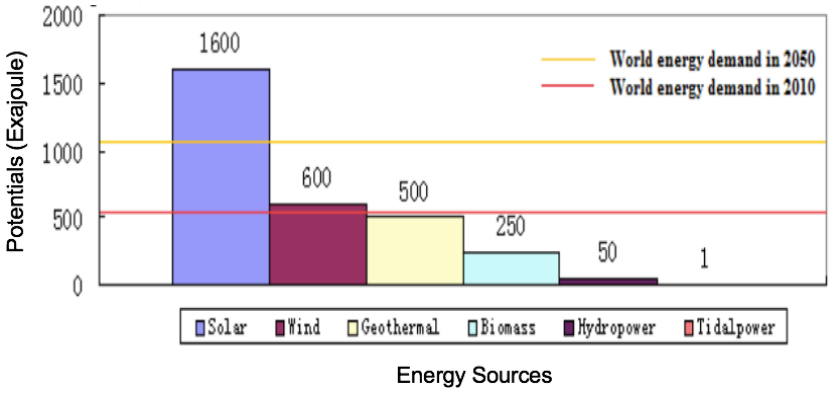

Figure1.1 Energy demand and available energy resources by 2050 [1.9].

1.2 Solar Cell Efficiency

One of the most important figures of merit for any type of solar cell, is efficiency. Figure 1.2 shows the best research-cell efficiencies compiled by NREL [1.10].

Lines with different colors indicated in Figure 1.2 show four categories of solar cells: multijunction III-V (GaAs, Ge/GaAs/InGaP, etc.) solar cells, crystalline Si cells, thin-film technologies, emerging PV. Notably, Si solar cells have the most contribution in the PV market yet.

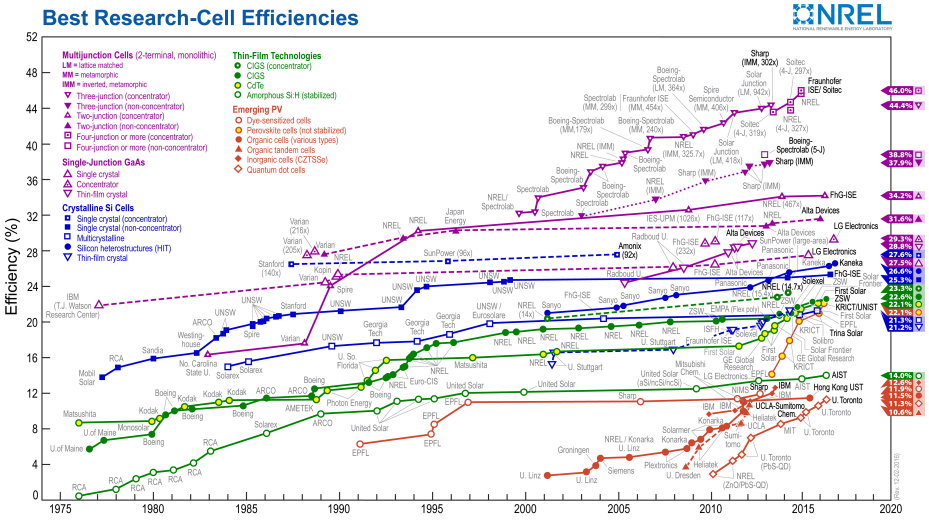

Figure 1.2 NREL compilation of best research solar cell Efficiencies [1.10].

1.3 Si Solar Cell Technology

The photovoltaic market is currently dominated by wafer based cryst alline silicon (Si) solar cells, and market share of thin-film cells is only about 10% [1.11]. This market share is due to the cell's high efficiency (~25% for single crystal Si), stability, and durability. However, wafer costs account for over 35% of the total module cost. M oreover, its material wastage is about 100 times greater than that of thin-film solar cells [1.12,1.13]. Silicon is an abundant material (about 2 5% of Earth's crust). It is non-toxic material,
which is especially important for a green technology. Si solar cell s have shown long-term stability over decades in practice (> 20 years).

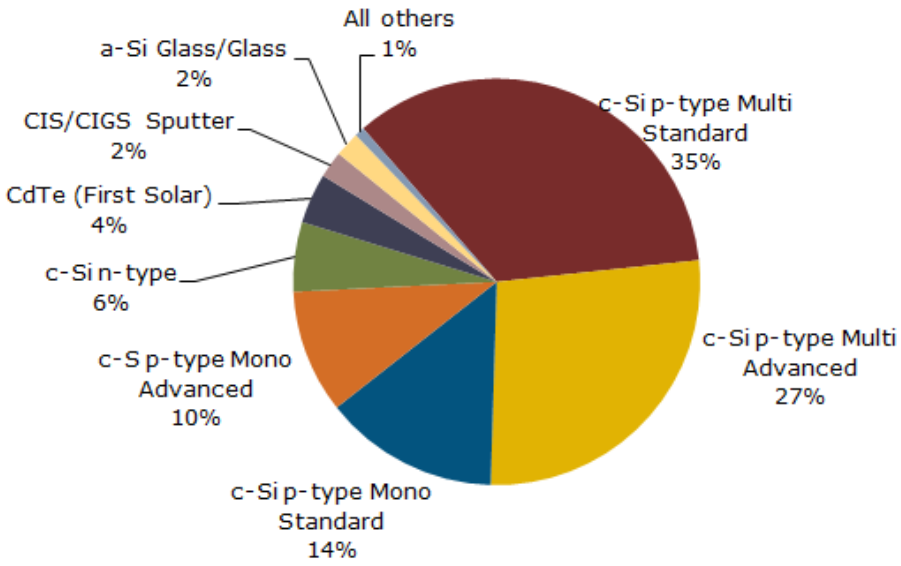

Figure 1.3 Contribution of Si solar cell and thin-film technologies in photovoltaic market at 2015 [1.14].

1.4 Thin-film Technologies for Solar Cells

Thin-film solar cells are less expensive and use easier to work with substrates (flexible and rigid) than the wafer based counterparts and hence produce lightweight and possibly flexible modules [1.15,1.16]. Most thin-film solar cells utilize glass substrate that technically enables the monolithic fabrication of large area devices through mature flat panel industry technologies [1.13]. Utilizing glass as a substrate of thin-film solar cells allows for promising low-cost solar cell technology. The flat panel display (FPD) industry, has scaled glass processing tools to an amazing 50 times higher throughput over the last few decades. All that know-how is available to anyone using glass substrate. However, the major limitation of thin-film solar cells is their lower efficiencies. Table

1.2, shows a list of typical thin-film solar cells and their best efficiencies.

Table 1.2 List of typical thin-film solar cells.

Thin-film Technology	World Record Efficiency
CIGS (CuInGaSe2)	19.5%
Amorphous Si	13.2% (not completely stabl e)
CdTe	16.5%

1.5 Thin-film Si Solar Cell

As the market size of photovoltaic modules continues to increase, raw material availability, manufacturing aspects, ecological considerations, and operational reliability will soon become crucial issues in selecting a thin-film photovoltaic technology [1.17,1.18]. Given the above-mentioned facts, thin-film Si occupies a special place among different thin-film photovoltaics. Moreover, the technology is unique because of well-established basics and strong synergy with the mature flat panel display industry [1.17] and has generated significant research interests since its development [1.19]. Extensive research efforts are underway in achieving innovative solutions and realizing both high performance and low costs for thin-film Si solar cells. The data are reported annually in efficiency tables [1.20]. Currently, the highest efficiencies for different types of solar cells ranges from 20% to 46%, depending on the nature of the photovoltaic materials used and device structure [1.21].

Chapter 2. Solar Cell principles and Background

2.1 Basic Solar Cell Parameters J_{SC}, V_{OC}, FF

2.1.1 Short-Circuit Current (J_{SC})

The short-circuit current is the current through the solar cell when the voltage across the solar cell is zero (i.e., when the solar cell is short circuited). Usually written as I_{SC} or J_{SC} (current density), the short-circuit current is shown on the I-V curve below. The short-circuit current is due to the generation and collection of light-generated carriers and is directly related to the absorption of solar cell device, since only light that is absorbed can be converted into current. In addition, the depletion width and the carrier diffusion lengths also greatly affect short-circuit current. If the depletion width is wider, and/or the diffusion length is longer, then a larger fraction of the photo generated electron-hole pairs will be swept by the built-in electric field in the depletion region, thus collected as current. On the other hand, if the depletion width is narrower and the diffusion lengths are shorter, then only a smaller fraction of the electron-hole pairs will be swept by the electrical field in the depletion region before electron-hole recombination. This recombination event occurs as a result of an excess electron in p-type material recombining with a hole, or an excess hole in an n-type material recombining with an electron. Since the depletion width is directly related to the background doping density, the short-circuit current is also affected by the background doping concentration in the depletion region [2.1, 2.2].

For an ideal solar cell at most moderate resistive loss mechanisms, the short-circuit current and the light-generated current are identical. Therefore, the short-circuit current is the largest current which may be drawn from the solar cell (Figure 2.1).

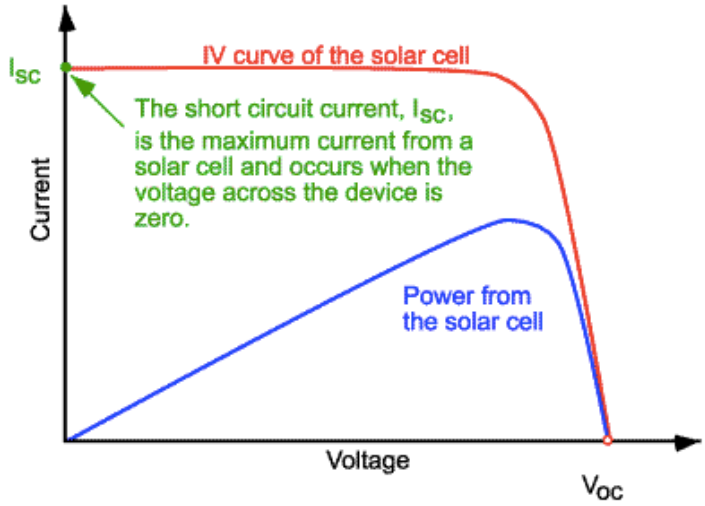

Figure 2.1 I-V curve of a solar cell showing the short circuit current [2.2].

2.1.2 Open-Circuit Voltage (V_{OC})

The open-circuit voltage, V_{OC}, is the maximum voltage available from a solar cell, and this occurs at zero current. The open-circuit voltage corresponds to the amount of forward bias on the solar cell due to the bias of the solar cell junction with the light-generated current.

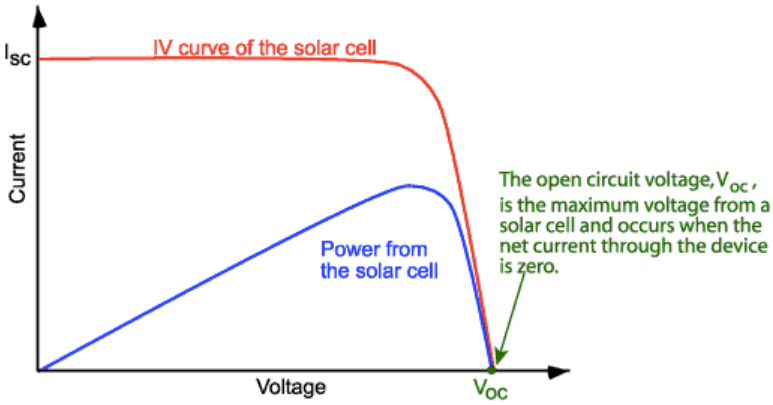

Figure 2.2 I-V curve of a solar cell showing the open-circuit voltage [2.3].

An equation for V_{OC} is found by setting the net current equal to zero in the solar cell equation to give:

$$V_{OC} = \frac{nKT}{q} \ln \left(\frac{I_L}{I_0} + 1\right) \tag{1.1}$$

The above equation shows that V_{OC} depends on the saturation current of the solar cell and the light-generated current. While I_{SC} typically has a small variation, the key effect is the saturation current, since this may vary by orders of magnitude. The saturation current, I_0 depends on recombination in the solar cell. Open-circuit voltage is then a measure of the amount of recombination in the device. Si solar cells on high quality single crystalline material have open-circuit voltages of up to 730 mV under one sun and AM1.5 conditions, while commercial devices on multicrystalline silicon typically have open-circuit voltages around 600 mV.

2.1.3 Fill Factor (FF)

The short-circuit current and the open-circuit voltage are the maximum current and voltage respectively from a solar cell. However, at both of these operating points, the power from the solar cell is zero. The "fill factor", more commonly known by its abbreviation "FF", is a parameter which, in conjunction with V_{OC} and J_{SC}, determines the maximum power from a solar cell. The FF is defined as the ratio of the maximum power from the solar cell to the product of V_{OC} and J_{SC} [2.4].

2.2 p-n Diode Versus p-i-n Diode

To have an electric field for electron hole separation, solar cells are formed as diode, p-n for crystalline and pin for thin-film. The internal electric field is limited to depletion region in p-n diode, however it extends over the whole intrinsic region in p-i-n type. The transport properties of photo-generated carriers in both amorphous and poly Si are far inferior compared to crystalline Si. As a result, excess carriers recombine within a very short distance from their origin (within distance much shorter than cell thickness). [2.5]

The principle of any solar cell is the separation of electron-hole pairs by the action of an internal electric field. The location of this electric field is governed by the requirement that all photo-generated carriers can travel sufficiently far to reach that field. In crystalline Si, solar cells this travel distance is determined by the carrier diffusion length, which is of the same order of magnitude as the cell layer thicknesses. The electric field, concentrated within the depletion layer of p and n layers, i.e., within a very thin zone of p/n junction is within reach for all the photo-

generated carriers which have to be separated (Figure 2.3). Thus, crystalline Si solar cell works as a p-n diode. However, due to extremely short travel distances of photo-generated carriers in a-Si and poly-Si, the electric field needs to present at the origin of photo-generation, in order to assist carrier travel and 'immediately' separate electrons and holes and thus, to avoid their recombination. The field assisted travel distance is governed by the drift length. For optimum utilization of the incident irradiance the electric field must extend throughout the entire cell thickens (vertical). This is accomplished by inserting an intrinsic region between p and n layers, whereby a p-i-n diode is formed [2.5].

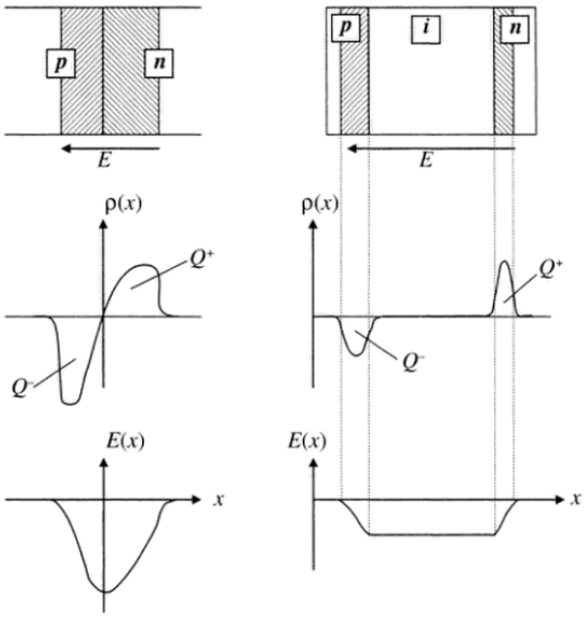

Figure 2.3 Built-in electric field, and depletion or space charge regions in p-n and p-i-n diode [2.5].

2.3 Properties of p-i-n-type Solar Cells

Figure 2.4 (a), (b), (c), and (d) show respectively, two- dimensional view of p-i-n diode, energy band diagram, space charge regions, and built-in electric field. The main difference between p-n diodes and p-i-n diodes is the extension of the internal electric field in the diode. In the case of the p-n diode, collection is governed by the minority carrier diffusion length L_{diff}. However, in p-i-n diode, collection is governed by the drift length L_{drift} of both electron and holes within i-layer that has a value of about 10 times larger than the minority carrier diffusion length [2.5]. The internal electric field, which extend throughout the photovoltaic intrinsic layer (Figure 2.4 (d)), is a key feature of p-i-n-type solar cells.

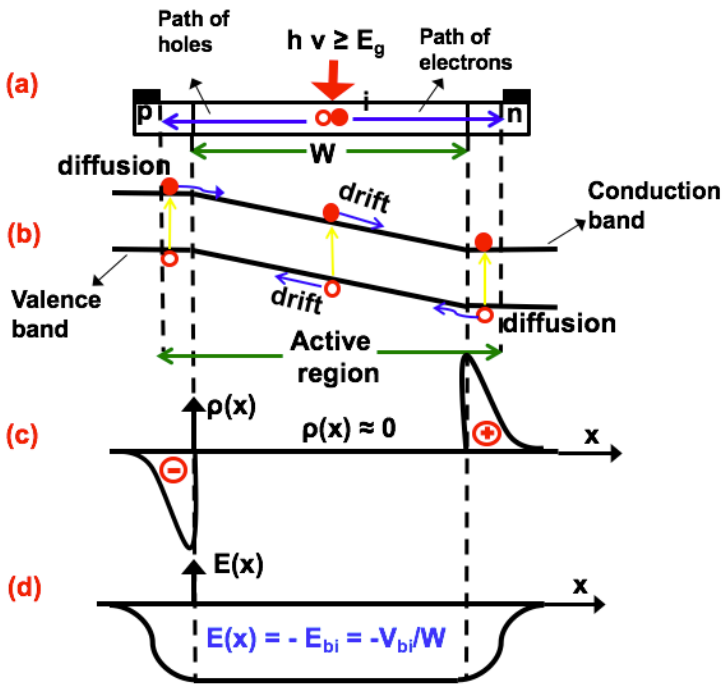

Figure 2.4 (a) Two-dimensional view of p-i-n diode, (b) energy b and diagram, (c) space charge regions, (d) Built-in electric field.

2.4 Conventional (Vertical) p-i-n Solar Cells Versus Lateral p-i-n Solar Cells

In this study, a laterally structured p-i-n diode is suggested for Si solar cell application. Conventional vertical thin-film p-i-n solar cells have two common configurations regarding deposition sequence of layers (Figure 2.5). The superstrate design of Figure 2.5 (light enters through the substrate) is particularly suited to building-integrated solar cells in which a glass substrate can be used as an architectural element. The substrate design has generally been applied to solar cells using flexible, stainless steel (SS) substrates. The detailed construction of a deposition facility of course depends upon whether the substrate is rigid or flexible.

Finally, it turns out that there is a profound effect of the substrate upon the properties of the first photodiode layers deposited upon it; this effect has led to fairly different photodiode structures for the superstrate and substrate designs [2.6].

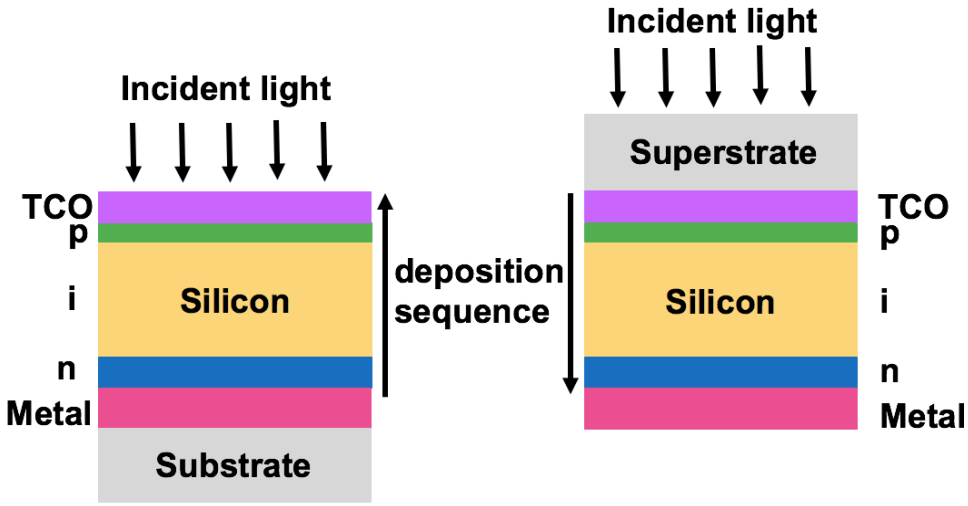

Figure 2.5 Two common vertical or conventional thin-film solar c ells; substrate and superstrate.

The schematic of the lateral structure can be seen in Figure 2.6. We believe that the lateral configuration of p-i-n layers is advantageous for solar cells because of the following fundamental reasons.

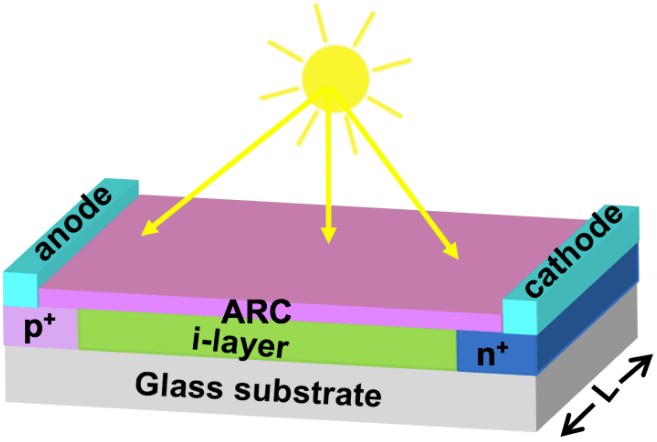

Figure 2.6 Three dimensional view of the lateral p-i-n silicon solar cell on glass substrate.

First, in the lateral solar cell, light directly acts on the photoactive region or absorber layer (i-layer). However, in the conventional vertical structures, incident light must pass through the glass substrate, front transparent conductive oxide (TCO), and p-type window layer before the intrinsic region is reached. Thus, a significant amount of the light may be absorbed or reflected within these layers, which do not contribute to the photo-generated current rather than photoactive intrinsic region [2.5]. The thin-film Si solar cells mainly posses a relatively low band gap value and are therefore destined to absorb light in the near-infrared region, where TCO has increased absorption because of free carrier absorption effects and results in increased absorption loss [2.7]. The front TCO layer presents the dominant source of absorption loss in thin-film Si solar cells [2.8]. Moreover, the incident light is partially reflected at TCO/p-type

interface before being mostly absorbed in the photoactive intrinsic region [2.9].

Second, the front p-type or window layer is not photoactive and causes optical absorption and electrical series resistance losses [2.5]. The window layer must be transparent as possible to the intrinsic region. However, the requirement for a sufficiently built-in electric field, does not allow a decrease in thickness below a certain value. By contrast, in the lateral cell, the window layer is removed from the front surface and placed in the side of intrinsic region.

Third, the lateral cell more efficiently uses light across the solar spectrum by adopting a wide intrinsic region, in which the main portion of photon absorption and photo carrier generation occurs (Figure 2.7). In the conventional vertical cells, the wide intrinsic region can be obtained by increasing device thickness. However, raising the thickness of thin-film cells involves technological and economical limitations [2.10].

Forth, the lateral cell benefits from one side contact, which is useful for cells integration simply by designing an interdigitated contact pattern [2.11-2.13].

Fifth, the lateral cell with appropriate thickness can be utilized in bifacial irradiation mode without using a rear reflector. Utilizing both front and ambient light surrounding the solar panel boosts the overall efficiency [2.13]. Moreover, the panel absorbs less heat than those conventional cells because of the former's much smaller area covered with metal.

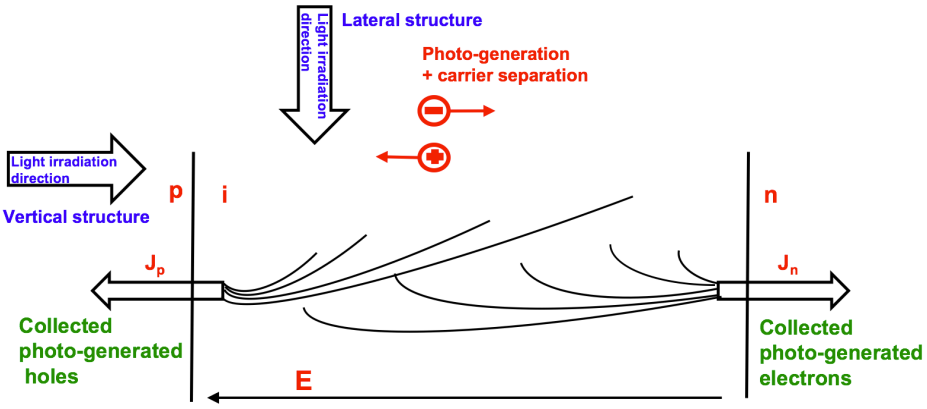

Figure 2.7 Photon absorption and photo carrier generation inside of the intrinsic region, p/i and n/i interfaces. It is assumed in this figure that light is uniformly absorbed in intrinsic region and recombination is negligible.

Chapter 3. Computer Simulation

The lateral structure of the p-i-n diode was characterized for thin-film Si solar cell application. As mentioned in pervious chapter, this structure can benefit from a wide intrinsic layer, which may improve efficiency without increasing cell thickness. Compared with conventional thin-film p-i-n cells, the lateral structure exploited direct light irradiation on the absorber layer, and one-side contact. Considering the effect of different carrier lifetimes and recombination, efficiency parameters were calculated by using a commercially available simulation program [3.1] as a function of intrinsic layer width, as well as the distance between p/i or n/i junctions to contacts. Excellent parameter values of 706.52 mV open-circuit voltage, 24.16 mA/Cm^2 short-circuit current, 82.66% fill factor, and 14.11% efficiency were obtained from a lateral cell (thickness = 3 μm; intrinsic layer width = 53 μm) in monofacial irradiation mode (i.e., only sunlight from the front side was considered). Findings of this work confirmed that the laterally structured p-i-n cell can be a potentially powerful means for producing highly efficient, silicon solar cells.

In this chapter, design, simulation and characterization results of lateral p-i-n solar cell is presented. In order to study optical and electrical characteristics of lateral p-i-n Si solar cell, FDTD Solutions, and the DEVICE simulator of a commercially available program were used.

3.1 Simulation Methodology

Design and characterization of the lateral p-i-n solar cell needs both optical simulations using FDTD Solutions and electrical simulations using DEVICE. (Figure 3.1) This is because the performance of any solar cell depends on not only optical absorption, but also charge transportation and the output electrical power.

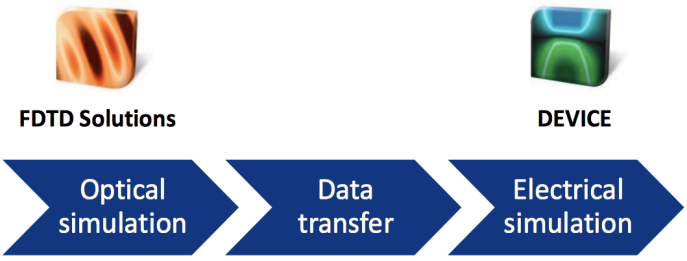

Figure 3.1 The flow of solar cell simulation using FDTD and DEVICE, used in this work [3.1].

The work flow of FDTD simulations can be summarized as below:

1. set the physical layout (geometry and materials)
2. add simulation region and boundary conditions, as well as meshing
3. add monitors, and the "solar_generation" analysis groups
4. run the simulation and then analyze the results
5. sweep or optimize some key parameters
6. generate data for the CHARGE solver
7. iterative simulation from CHARGE results

The geometry, simulation region, and solar_generation analysis group is shown in Figure 3.2.

In Figure 3.3, the schematic of optical and electrical structure of a lateral cell, with defining simulation region is shown. In the FDTD, a

unit cell is selected, then by setting “periods” number the whole device region will be covered in the simulation.

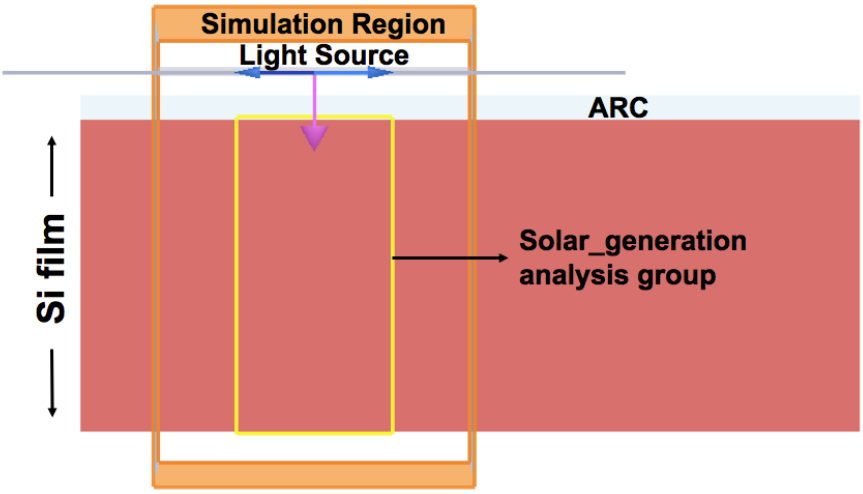

Figure 3.2 Schematic of the latera cell geometry and design in FDTD layout for optical simulation.

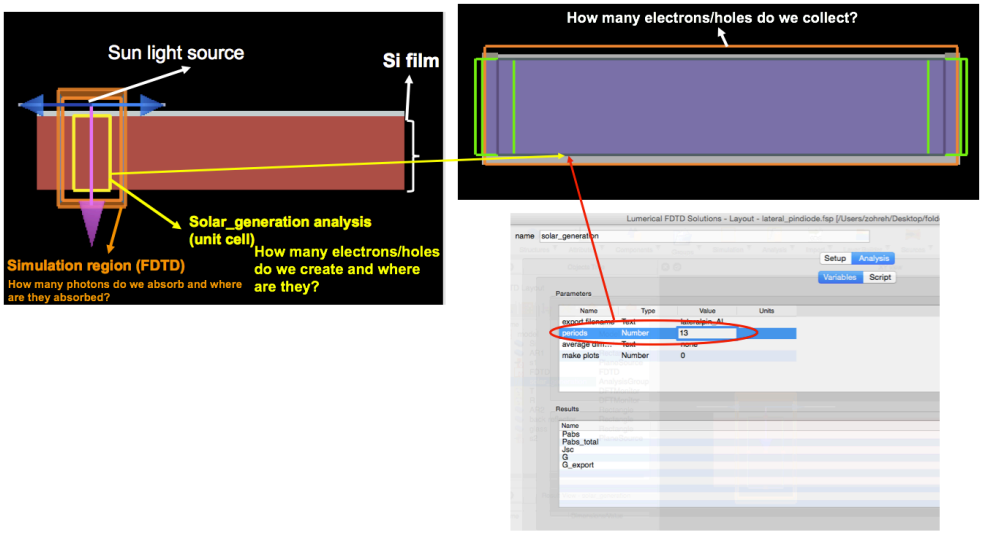

Figure 3.3 Simulation region definition in FDTD and DEVICE for optical and electrical simulation.

In following the physics and equations used in the simulators will be explained briefly.

3.1.1 Physics and Equations

FDTD calculates absorbed optical power per unit volume at each wavelength by solving Maxwell's curl equations:

$$\frac{\partial D}{\partial t} = \nabla \times H \tag{3.1}$$

$$D(\omega) = \varepsilon(\omega)E(\omega) \tag{3.2}$$

$$\frac{\partial H}{\partial t} = -\frac{1}{\mu}\nabla \times E \tag{3.3}$$

where H, E, and D are the magnetic, electric, and displacement fields, respectively, while ε is the complex relative dielectric constant. The FDTD method solves these equations on a discrete spatial and temporal grid. Each field component is solved at a slightly different location within grid cell (Yee cell, Figure 3.4), as shown below. By default, data collected from the FDTD solver is automatically interpolated to the origin of each grid point.

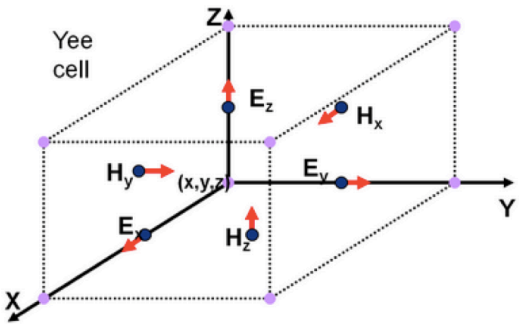

Figure 3.4 The grid cell or Yee cell [3.1].

After optical simulation, the data is transferred to the DEVICE for electrical stimulation based on charge transport. In continue, the basic mathematical and physics formalism behind the algorithm used in charge transport solver of the DEVICE will be introduced briefly. It starts from non-linear Poisson and drift-diffusion equations. DEVICE solves the drift-diffusion equations for electrons and holes (carriers)

$$J_n = q\,\mu_n\,n\,E + q\,D_n\,\nabla \mathrm{n} \tag{3.4}$$

$$J_p = q\,\mu_p\,n\,E + q\,D_p\,\nabla \mathrm{p} \tag{3.5}$$

Where $J_{n,p}$ is the current density (A/cm^2), q is the positive electron charge, μn,p is the mobility, E is the electric field, $D_{n,p}$ is the diffusivity, and n and p are the densities of the electrons and holes, respectively. Each carrier moves under the influence of two competing processes: drift due to the electric field, and random thermal diffusion due to the gradient in the density. These processes are represented in the drift-diffusion equations as the sum of two terms.

To solve the drift-diffusion equations, the electric field must be known. To determine the electric field, Poisson's equation is solved:

$$-\nabla.(\varepsilon \nabla V) = qp \tag{3.6}$$

where ε is the dielectric permittivity, V the electrostatic potential $(\mathrm{E} = -\nabla V)$ and ρ the net charge density,

$$p = p - n + C \tag{3.7}$$

which includes the contribution C from the ionized impurity density. Finally, the auxiliary continuity equations are required to account for charge conservation

$$\frac{\partial n}{\partial t} = \frac{1}{q} \nabla . J_n - R_n \tag{3.8}$$

$$\frac{\partial p}{\partial t} = \frac{1}{q} \nabla . J_p - R_p \tag{3.9}$$

where $R_{n,p}$ is the net recombination rate (the difference between the recombination rate and generation rate). The physical processes associated with the material are assumed to act equivalently when applied to electrons or holes, and as a result, $R = R_n = R_p$. The recombination and generation processes are important factors in the material-specific calculation of carrier behavior. Multiple recombination and generation processes are modeled, which may depend on temperature, impurity (doping) concentration, carrier concentration, electric field, and current density.

DEVICE discretizes and solves the drift-diffusion and Poisson's equations on an unstructured finite-element mesh in one and two dimensions. The simulation region is partitioned into multiple domains along boundaries between materials with unique physical descriptions. The materials used in the simulation may be categorized as insulators, semiconductors, or conductors; each type of material has an associated user-specified model or collection of models that describe its behavior. The system of equations solved by DEVICE admits both a steady-state and time-varying result. By enforcing the condition

$$\frac{\partial n}{\partial t} = \frac{\partial p}{\partial t} = 0$$

in the continuity equations, the carrier density and electrostatic potential can be solved at steady-state. Steady-state simulations can be used to examine the system's behavior at a fixed operating point. Alternately, by specifying an initial condition for the carrier density and electrostatic potential, the equations can be solved in a sequence of discrete times.

Boundary conditions are very important in an accurate semiconductor device simulation. Two categories of boundary condition are present in DEVICE: those that relate to the electrostatic potential (Poisson's equation) and those that relate to the carrier densities (the drift-diffusion equations). Poisson's equation and the drift-diffusion equations are second-order partial differential equations (PDE), and each requires that the solution be explicitly specified for at least one location.

3.1.2 Design and Parameters

Design parameters of the lateral p-i-n structure shown in Figure 3.5 is explained in this section. First a 3 μm thick (t = 3 μm) and a lightly doped p-type ($N_A = 10^{12}$ cm^{-3}) Si thin-film are selected instead of pure intrinsic Si as the i-layer. The film possessed a length L = 1 cm on a SiO_2 glass substrate. To define side electrodes, diffusion objects with Gaussian doping profile were used. The doping concentration of p- and n-type electrodes were selected as $N_A = N_D = 10^{19}$ cm^{-3}. The depth of p/i and n/i junctions was 0.2 μm. The width of both p- and n-type layers were set to $d_p = d_n = 1$ μm. The contacts were not located on the top of the intrinsic regionor p/i and n/i junctions. Hence, it is assumed herein the use of aluminum (Al) metal layers, which enables good ohmic contact to

both the highly doped p-type and highly doped n-type layers simultaneously [3.2, 3.3]. Then Al layers were used with width and thickness of 0.5 µm and 0.3 µm, respectively, as anode and cathode contacts. The distance between junctions and contacts was selected as d = 0.5 µm. Considering the above-mentioned parameters, simulations were performed efficiency parameters were calculated under standard test conditions, specifically, 100 mW/cm^2 incident power, 25 ^{o}C temperature, and AM 1.5 spectrum.

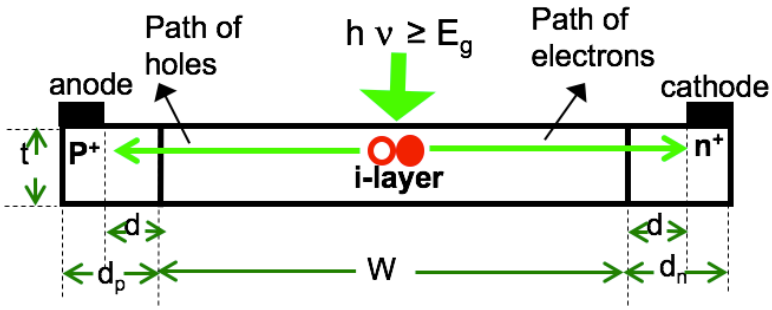

Figure 3.5 Two-dimensional view of the lateral p-i-n solar cell showing length, width and thickness.

Table 3.1 Design symbols and related description of the lateral cell, used in the simulation.

Symbol	Description
W	width of the i-layer
L	length of the i-layer
t	thickness of the i-layer
d	distance between contacts and junctions (p/i and n/i interfaces)
d_p ,d_n	width of p and n doped regions
τ	carriers lifetime
μ	carriers mobility
W_j	junction depth
N_D, N_A	doping concentration of n-layer and p-layer

All the above-mentioned design parameters are shown in Figure 3.5 and Table 3.1. Moreover, the band diagram of a lateral cell with W = 13 μm at zero applied voltage is displayed in Figure 3.6, where, E_c is the energy level of the bottom of the conduction band, E_v is the energy level of the top of the valence band, and E_i is the intrinsic Fermi level.

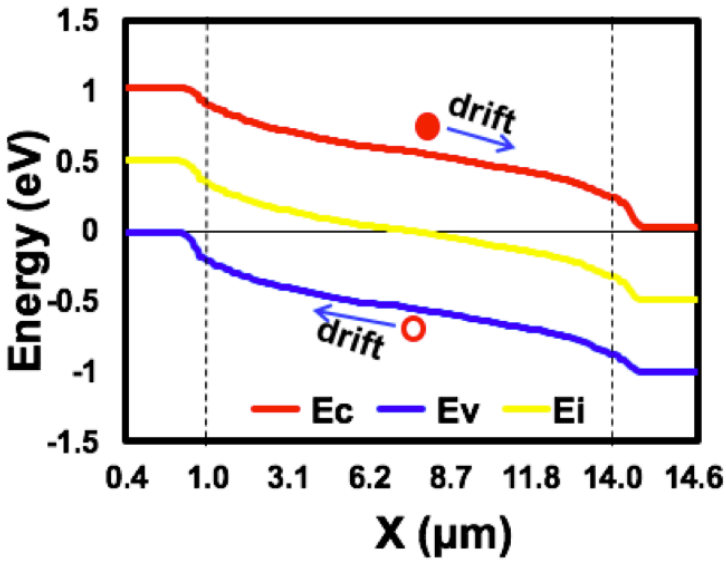

Figure 3.6 Energy band diagram of the lateral p-i-n cell with W= 53um.

3.2 Results and discussion

To demonstrate photovoltaic behavior of the laterally structured p-i-n cell, first the I–V curve of a lateral cell with W = 13 μm in the dark and under illumination was simulated. The obtained open-circuit voltage (V_{OC}) and total photo-generated current (I_{SC} or I_{ph}) from the illuminated I–V curve of Figure 2 shows that the lateral structure could be potentially a good choice for use in thin-film solar cell applications. The voltage and current of the maximum power (V_{mp} and I_{mp}), and maximum power point (P_{mp}) are displayed in the illuminated I–V curve. Notably, the currents and output power shown in Figure 3.7 are absolute values and have not been normalized to the area of the cell.

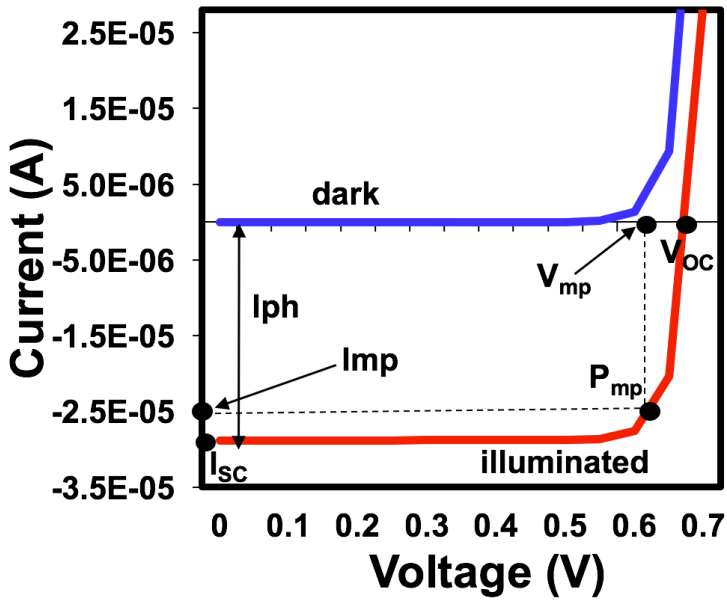

Figure 3.7. I–V curve of the lateral cell under dark and illuminated condition (W = 13 μm), showing V_{OC}, I_{SC}, V_{mp} and P_{mp}.

3.2.1 Effect of Antireflection Coating and Rear Reflector

A thin Sio_2 layer (0.15 μm) was adopted on the front surface of the lateral cell (W = 13 μm) to produce surface passivation and anti-reflection coating (ARC). Figure 3.8 (a) and (b) show the improvement of the short-circuit current density (J_{SC}) and output power density under the effect of ARC. The J_{SC} achievable by the ARC was 20.42 mA/cm^2, which corresponds to about 3.4 mA/cm^2 improvement relative to the J_{SC} of the lateral cell without ARC. Moreover, the output power increases from 9.71 mW/cm^2 to 11.73 mW/cm^2 because of the effect of ARC. Notably, all current and power density numbers of the figures are the normalized values by the area of the lateral cell. To obtain densities of

current and power, the total area of the lateral cells was considered, because almost the entire surface of the cell is active.

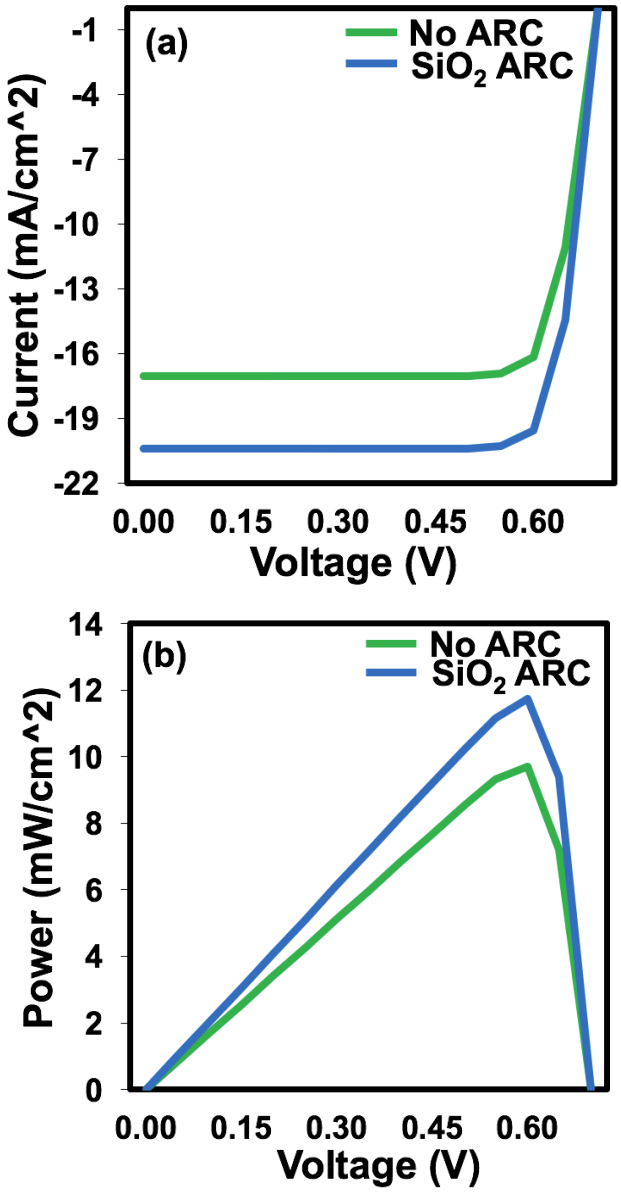

Figure 3.8 Comparison of (a) short-circuit current density (J_{SC}) and (b) output power density of the lateral cell with and without considering the effect of anti-reflection coating, (0.15 μm thick Sio2 ARC), (W = 13 μm).

The J_{SC} and output power density of the lateral cells were measured under the effect of using 0.3 μm thick Al and silver (Ag) rear reflectors, which are commonly used in thin-film Si solar cells. All of the three lateral cells in Figure 3.9 (a) and (b) benefit from that the ARC, and the rear reflector was considered at the bottom of the glass substrate. Figure 3.9 (a) presents the improvement in J_{SC} from 20.42 mA/cm^2 to 23.55 mA/cm^2 under the use of Al and 24.16 mA/cm^2 under the use of Ag as rear reflector. In Figure 3.9 (b), the output power density increases from 11.73 mW/cm^2 to 13.52 mW/cm^2 and 13.92 mW/cm^2 under the use of Al and Ag, respectively, as rear reflectors.

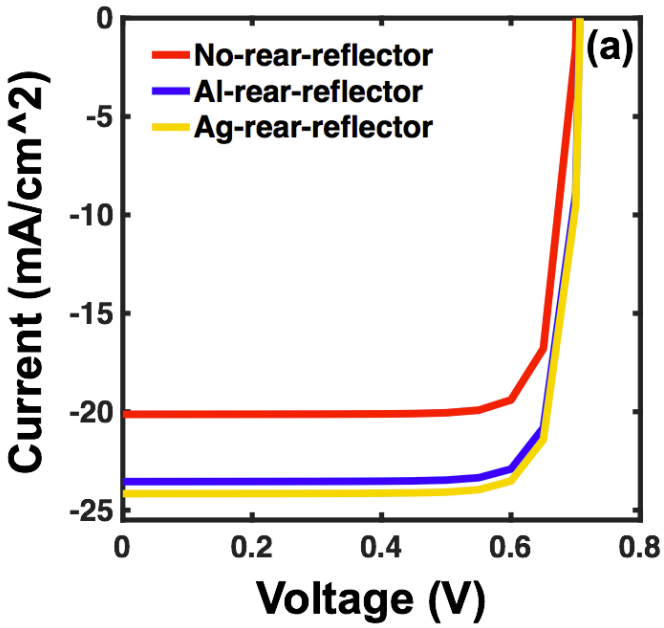

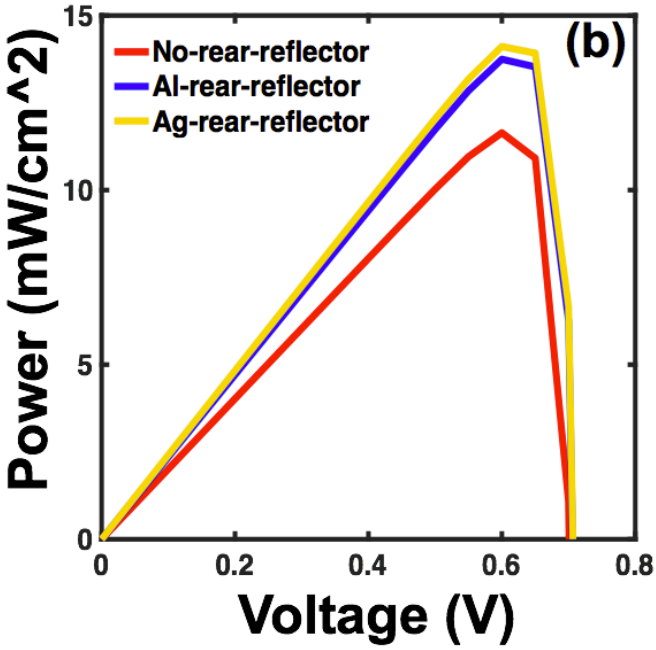

Figure 3.9. Comparison of (a) short-circuit current density (J_{SC}) and (b) output power density of the lateral cell with and without considering the effect of rear reflector. Considering the effect of 0.3 μm thick aluminum (Al) and silver (Ag) as the rear reflector, (W = 13 μm).

3.2.2 Effect of Doping and Dimension of p- and n-type Regions

In the lateral p-i-n solar cell, p- and n-type regions are located in the sides of intrinsic region. Hence, this structure has less limitation in selecting doping concentration and dimension of doped regions, compared to the conventional vertical p-i-n cells.

It should be mentioned that in vertical cells, smaller dp and dn are desired. However, it cannot be reduced below certain minimal values, otherwise sufficient space charge cannot be formed. This issue is

particularly important for p layer (window layer) in vertical [3.4]. If the thickness of intrinsic region reduced, the E_{bi} increased with the given (V_{bi}) so the minimal width of doped layers must be increased to provide sufficient areal charge density to support the stronger electric field.

In this section, different doping concentrations and dimensions were assumed and I-V curve of a lateral cell with W = 13 µm simulated. Results in Figure 3.10 showed that V_{OC} increased by increasing doping of p- and n- type layers. The V_{oc} enhancement caused by reduced diode saturation current (enhanced built-in voltage) with increased dopant density of electrodes. Figure 3.11 shows I-V curves of the lateral cell with assuming doped region widths from 1 µm to 0.6 µm (dp and dn). It can be seen from this figure; V_{OC} reduces by reducing dp and dn. The reason is the reduction in E_{bi} that is shown in Figure 3.12.

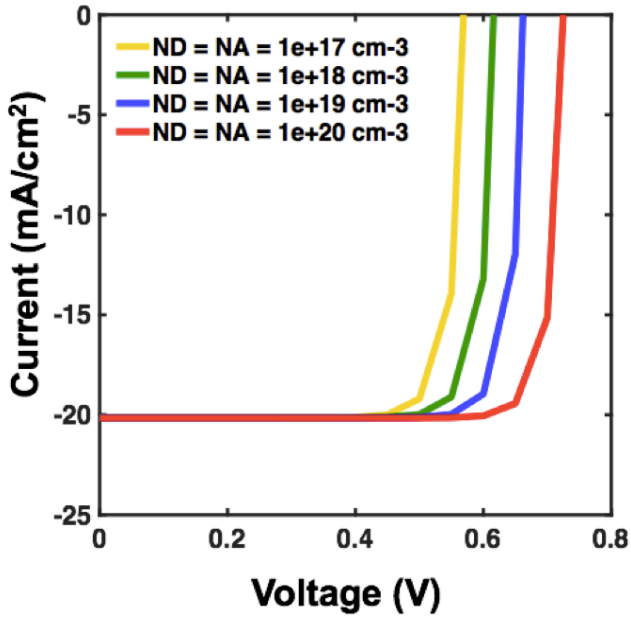

Figure 3.10 Effect of doping concentration of p- and n-type regions on the I-V curve of the lateral cell.

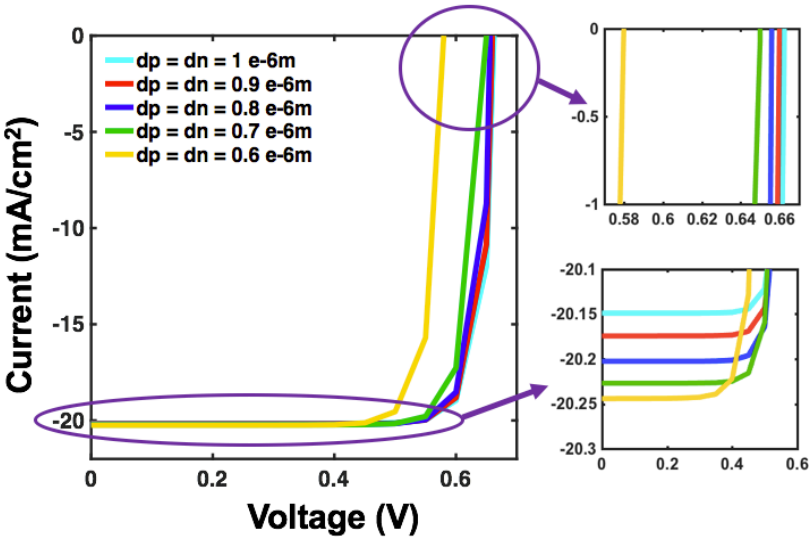

Figure 3.11 Effect of dimension (width) of p- and n-type regions on the I-V curve of the lateral cell.

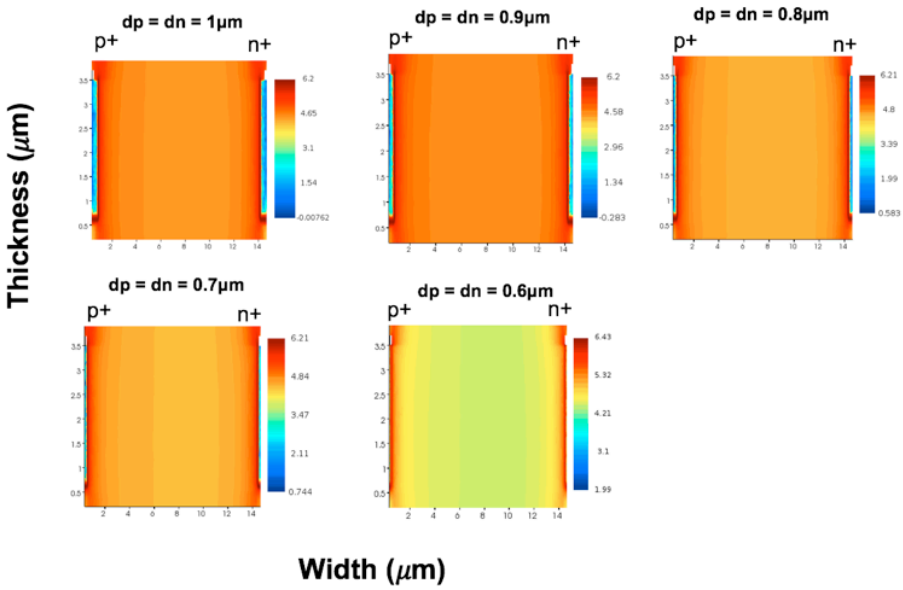

Figure 3.12 Built-in electric field, E_{bi} of the lateral cells with different width of p- and n- type layers (in the Log scale).

3.2.3 Effect of Materials Quality

Recombination of the photo generated carriers is an efficiency limiting factor in any type of solar cell. The dominant bulk recombination mechanisms in Si solar cells are Auger, and Shockley-Read-Hall (SRH) via defect states [3.5]. Thus, in this section the effect of these recombination mechanisms on the I-V curve of the lateral solar cell is presented.

Auger recombination is dominant under high-level injection condition, due to its dependence on the cube of carrier density. (specially observed in concentrator solar cells). The most widely used values for the Auger coefficients are those measured by Dziewior and Schmid in heavily doped silicon and Svantesson and Nilsson in highly injected silicon [3.6, 3.7]. These coefficients are in good agreement, 3.8 and 3.88 × 10^-31 cm^6/s, respectively, if the ambipolar coefficient is taken to be the sum of the individual coefficients in p-type and n-type silicon. Both of these experiments determined the recombination rates primarily at carrier densities above 10^18 /cm3 where this recombination clearly dominates over the other recombination processes [3.8, 3.9].

Considering typical values for carrier lifetime of SRH and carriers capture coefficient of Auger recombination in the literature, the following numbers were assumed for simulation of Figure 3.13.

SRH1; Shockley-Read-Hall recombination with carrier lifetime, τ = 100 e-6 s

SRH2; Shockley-Read-Hall recombination with carrier lifetime, τ = 10 e-6 s

SRH3; Shockley-Read-Hall recombination with carrier lifetime, τ = 3.3 e-6 s

Auger1; Auger recombination with carrier capture coefficients

Electrons: 2.8e-30 cm^6/s

Holes: 9.9e-31 cm^6/s

Auger2; Auger recombination with carrier capture coefficients

Electrons: 2.8e-31 cm^6/s

Holes: 9.9e-32 cm^6/s

The results of Figure 3.13 show that the change in J_{SC} is small. However, V_{OC} reduces under the effect of bulk recombination, specifically under the effect of SRH. Hence, the I-V and P-V curves of the lateral cell with considering different SRH carrier lifetime were simulated in Figure 3.14.

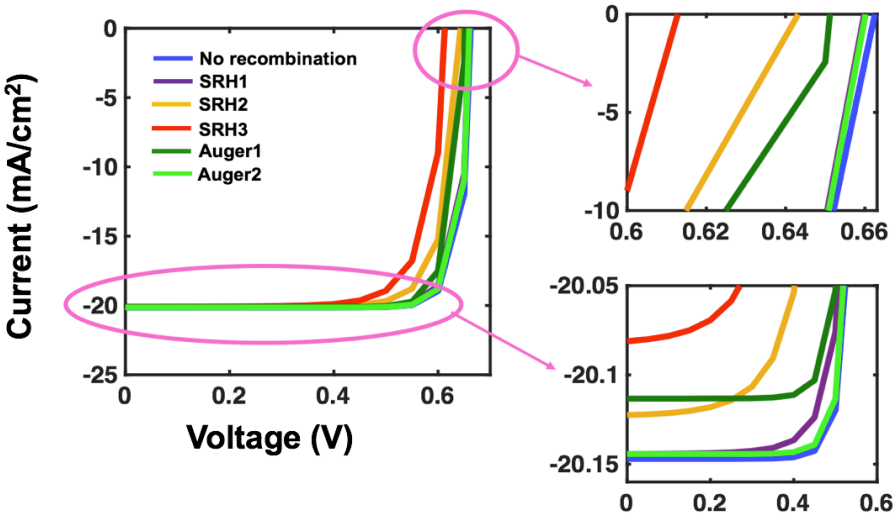

Figure 3.13 Effect of Bulk and Auger recombination on the I-V curve of the lateral cell with W = 13μm.

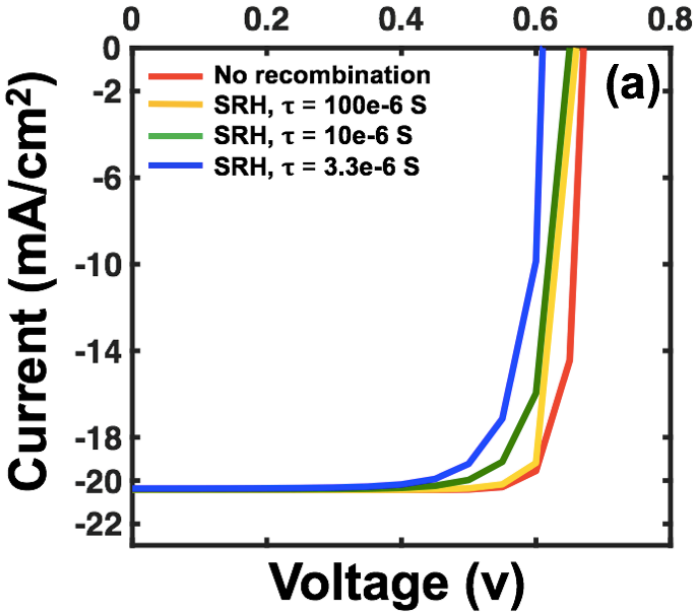

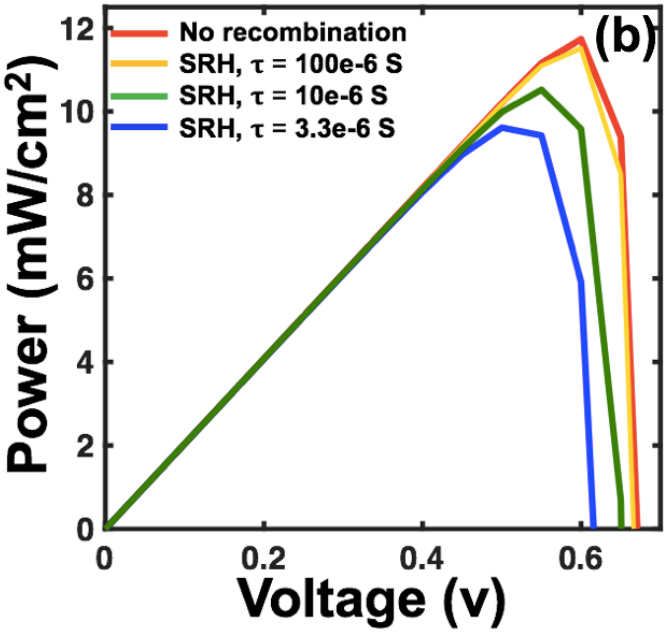

Figure 3.14 (a) I-V and (b) P-V curves of the lateral cell with W= 13 µm, assuming different carrier lifetime under the effect of SRH recombination.

3.2.4 Parameters of Drift Mechanism: Built-in Voltage and Built-in Electric Field

The main transport mechanism of charged carriers in p-i-n diode is drift, due to the existence of built-in electric field in intrinsic region. Hence, drift length of carriers is an important factor in efficiency of p-i-n solar cells. Drift length is function of carrier's lifetime, carrier's mobility, and built-in electric field ($L_{drift} = \tau\ \mu\ E_{bi}$). Built-in electric filed ($E_{bi} = |V_{bi}/W|$) is function of built-in voltage (V_{bi}) and inversely proportional to the intrinsic region width (W). Thus, in this section V_{bi} and E_{bi} of lateral cell is simulated for W = 3, 13, 53, and 203 µm. Figure 3.15 shows V_{bi} of lateral p-i-n cells, assuming no applied bias voltage

and dark condition. The built-in voltage is sum of p/i and n/i interfaces voltage that is about 1V for Si material.

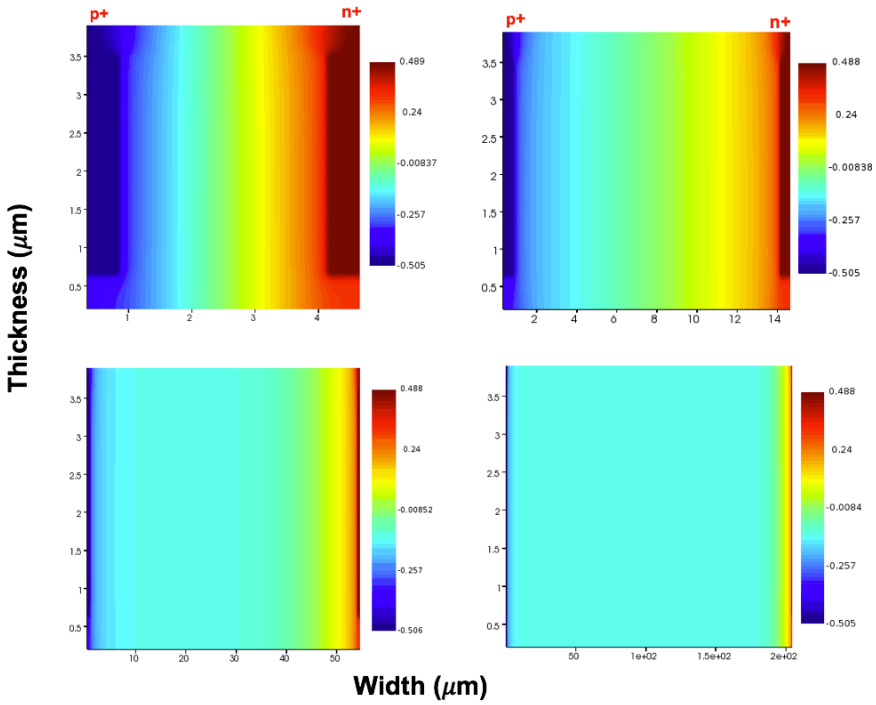

Figure 3.15 Built-in voltage of lateral p-i-n cells with different value of W, assuming dark condition and zero applied voltage.

The strength and distribution of built-in electric field is essential in photo-generated carrier's separation and transport in the intrinsic region of the p-i-n solar cells. For the optimum utilization of the incident irradiance, the electric field must extend throughout the entire intrinsic region with sufficient strength. Hence, we simulated a wide lateral cell with W = 53 μm, to check the distribution and strength of the E_{bi} at the junctions and middle of the i-layer. Figure 3.16 (a) and b depict two dimensional distributions of the E_{bi}, respectively, in darkness and

illumination and in the log scale for lateral cells with W = 3, 13, 53, and 203 µm. Under dark condition, the electric field was very high near p/i and n/i junctions and dropped quickly with distance from electrodes. However, light illumination altered the electric field behavior and became sufficiently high at the middle of the intrinsic region. It can be seen that E_{bi} reduces by widening intrinsic region. However, even for very wide lateral cell (W = 203 µm) it is still sufficiently strong to separate charged carriers. The strength of the E_{bi} is substantially important for the lateral cells with wide or ultra-wide i-layer. This property can be increased by selecting proper doping concentrations and widths of p- and n-type regions [3.4].

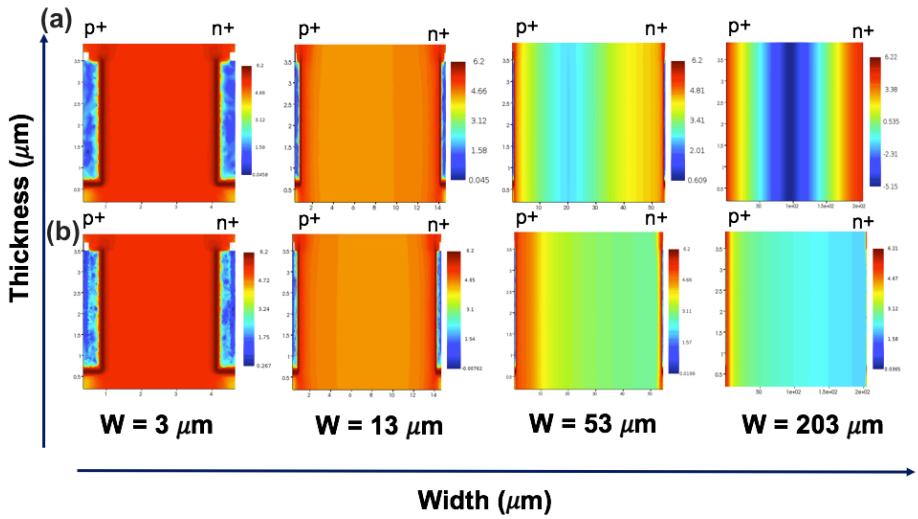

Figure 3.16 The built-in electric field (E_{bi}) (a) under dark and (b) light illumination.

3.2.5 Effect of Intrinsic Region Width on Efficiency Parameters

The effect of intrinsic regionwidening on the efficiecny parameters of the lateral cells was evaluated with considering different Si material qualities. For this purpose, lateral cells with and without recombination were simulated while assuming different carriers lifetimes. The dominant bulk recombination mechanism in Si solar cells is the Shockley-Read-Hall (SRH) via defect states [3.5]. Thus, only SRH recombination was considered for the simulations of this section. For all lateral cells, the same value of carriers mobility (~400 $cm^2/(V \cdot s)$) was assumed, and then increased the width of the intrinsic region from very narrow (W = 1 μm) to ultra wide (W = 248 μm). In Figure 3.17, the J_{SC} of all the lateral cells are close to one another and increase with a relatively steep slope after the intrinsic regionwas widen from 1 μm up to 13 μm.

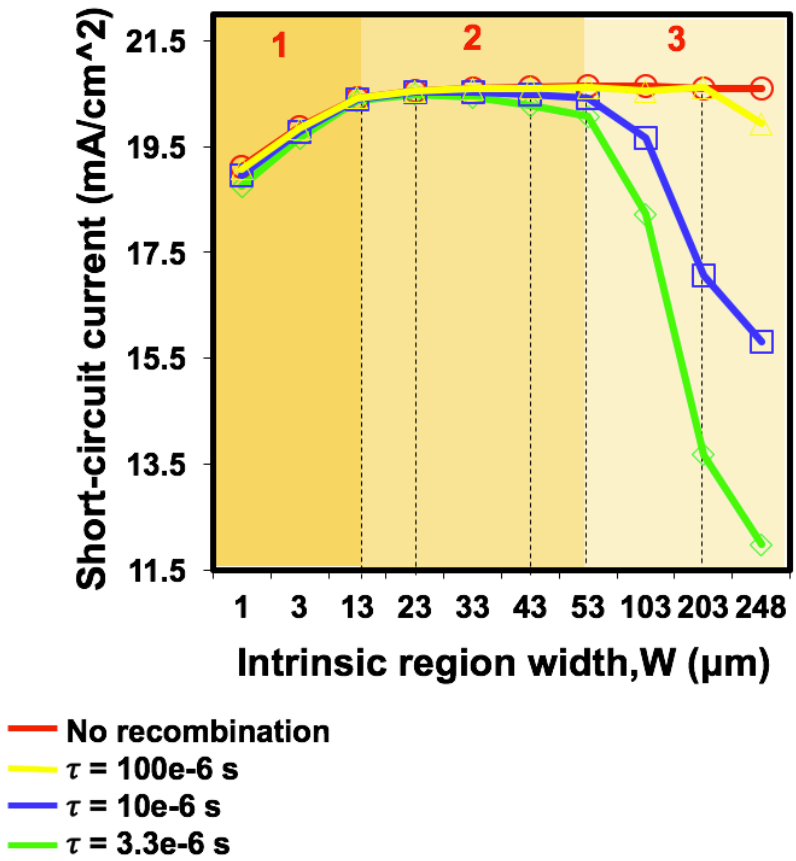

Figure 3.17 Short-circuit current density as the function of intrinsic region width and τ as a parameter.

For W < 13 μm, current increases rapidly, because of photon absorption enhancement, and consequently photo-carrier generation enhancement as the result of increasing intrinsic region width. The main portion of photo curent is generated in the intrinsic region of the p-i-n cells [3.4], [3.10], and the layer is directly exposed to the incident light in the lateral structure. However, the improvement of the J_{SC} continues with a gentler slope beyond W = 13 μm up to the specific values of W depending on the carrier lifetimes of the lateral cell. For examle, for the

lateral cell with τ = 3.3, 10, and 100 μs, increasing the intrinsic region width to beyond W = 33, 53, and 203 μm, respectively, will not add benefit to the J_{SC}. The decrease in J_{SC} for the ultra-wide lateral cell can be explained by the path length along which charge carriers must travel for collecttion in the electrodes.The path length increases with the wider intrinsic region, which results in increased series resistance and recombination of carriers. The results confirm that the decrease in J_{SC} of ultra-wide lateral cells becomes significant as the recombination increases (reduced τ).

To benefit from intrinsic region widening in the lateral structure, one should consider that the carrier drift length ($L_{drfit} = \tau\ \mu\ E_{bi}$) must be larger than the W. In narrow lateral cells, e.g., cells with W less than 13 μm, the electric field is sufficienly high; hence, the drift length can be larger than W even at low τ. For Ws less than 13 μm, the effect of τ on the J_{SC} is negligible. However, for larger Ws, the electric field reduced, and τ became effective and played an important role in the J_{SC} of specifically ultra-wide lateral cells with W larger than 53 μm.

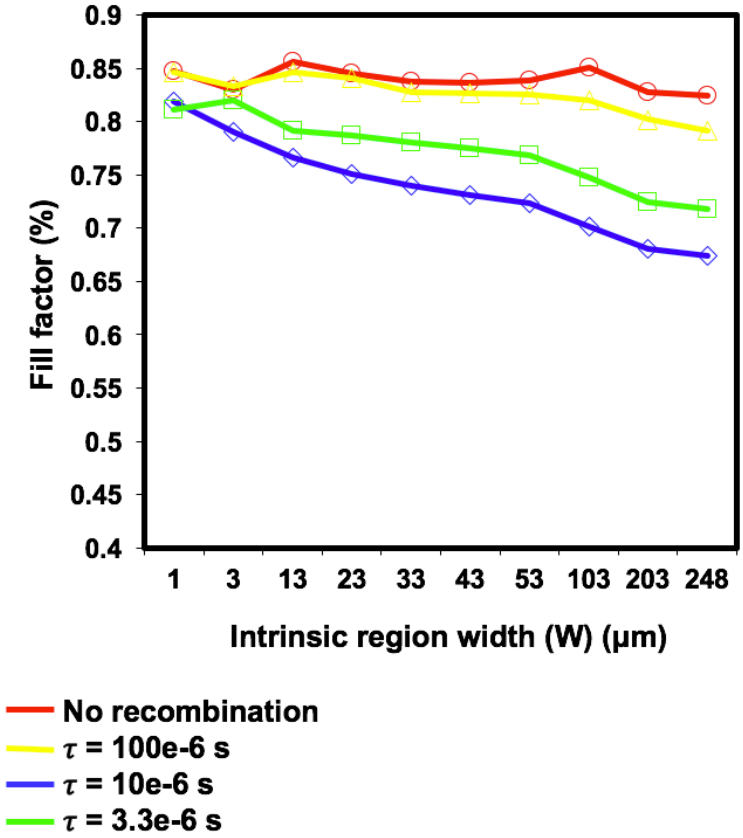

Figure 3.18 Fill factor as the function of intrinsic region width and τ as a parameter.

Figure 3.18, shows the fill factor as the function of W with τ as parameter. For the lateral cell with no recombination, a small fluctuation around 0.85 was observed for all values of W from 1 μm to 248 μm. For the lateral cell with τ = 100 μs, the fill factor fluctuated around 0.83 for the W from 1 μm to 53 μm, and decreased for larger Ws. For the lateral cells with τ = 10 and 3.3 μs, the fill factor diminished from 0.8 to 0.71 and 0.67, respectively, by increasing W from 1 μm to 248 μm. The decrease in fill factor may be described similarly to the decrease in the J_{SC}.

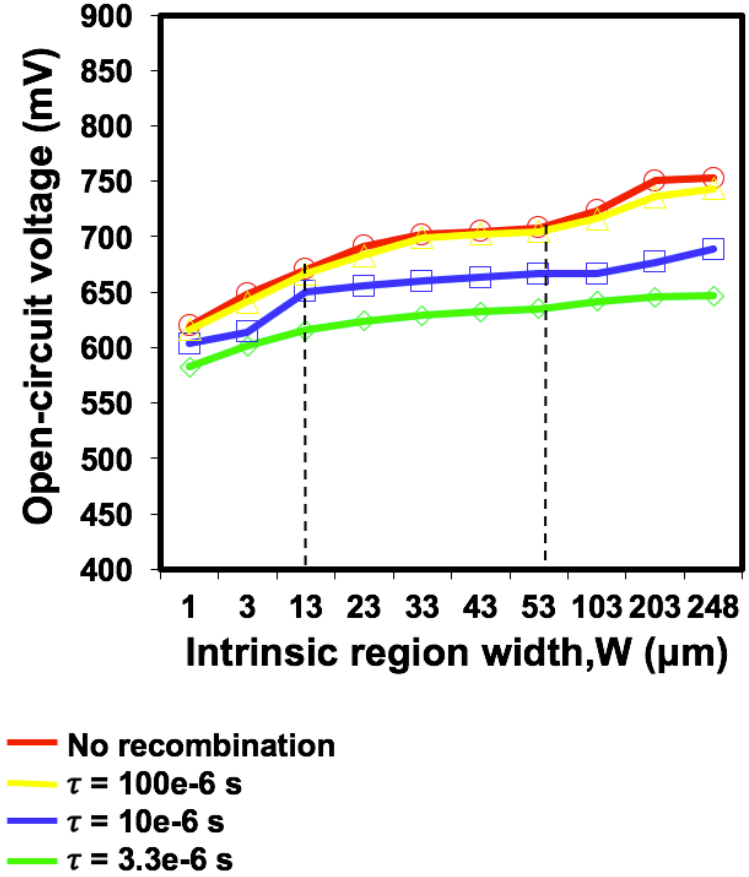

Figure 3.19 Open-circuit voltage as the function of intrinsic region width and τ as a parameter.

Figure 3.19, shows the V_{OC} as the function of the W with τ as a parameter. The V_{OC} increases by more than 100 mV by increasing W from 1 μm to 248 μm for lateral cells with no recombination and τ = 100 μs. The V_{OC} of the lateral cells with mediocre and low carrier lifetime (e.g. τ = 10 μs and 3.3 μs), increased to about 80 mV and 60 mV, respectively, by increasing W from 1 μm to 248 μm. This improvement mainly attained through W widening up to 13 μm. Beyond this point,

V_{OC} exhibited a small change. V_{OC} is a measure of carrier recombination (and hence τ) in the solar cell. Thus, the lateral cells with different τ showed different values of V_{OC} at any W. However, this difference was minimum (34 mV) at W = 1 μm, and maximum (106 mV) at W = 248 μm. This observation was achieved because the effect of τ increased by increasing the W and consequently reducing the E_{bi}.

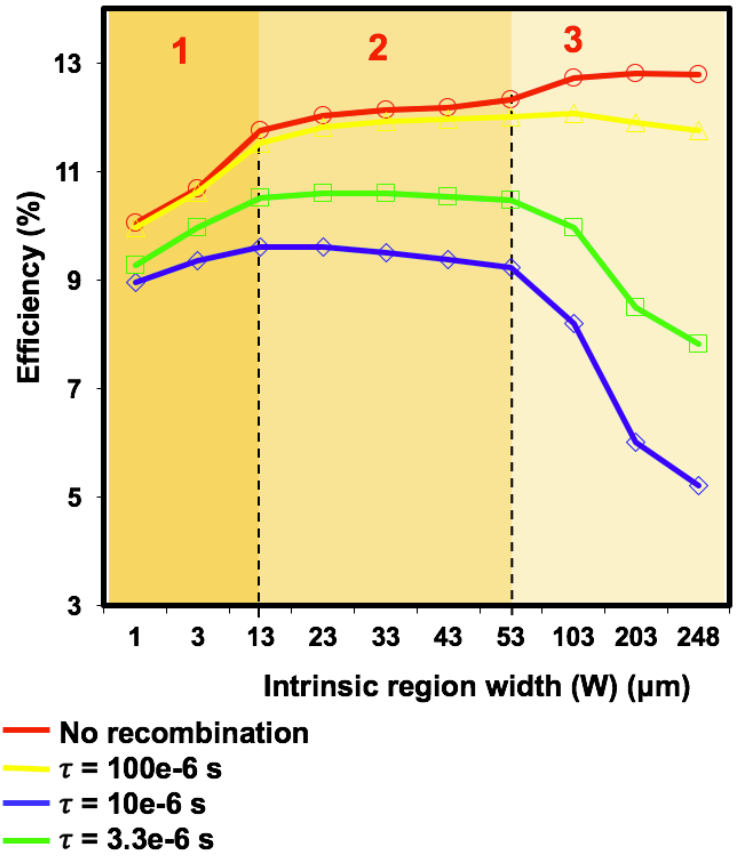

Figure 3.20 Efficiency as the function of intrinsic region width and τ as a parameter.

The combined effect of the intrinsic region width on the J_{SC}, V_{OC}, and

fill factor is shown in Figure 3.20. As predicated, the efficiency of all the lateral cells increased by the intrinsic region widening of up to 13 μm but with steeper slope for lateral cells with no recombination and τ = 100 μs. The total efficiency improvement for the lateral cells with no recombination τ = 100, 10 and 3.3 μs were 2.7%, 1.7%, 1.3%, and 0.7%, respectively. These improvements were mainly attained by W widening to up to 13 μm. The efficiency of the lateral cells with τ =10 and 3.3 μs did not virtually change with W variation from 13 μm to 53 μm and began to decrease beyond 53 μm. Given the results in Figure 3.20, it can be concluded that intrinsic region widening is significantly beneficial if a reasonable carrier lifetime is considered. The widening of the intrinsic region of the lateral structure can be compared with the thickening of the intrinsic regionin the conventional cells with vertical configuration of the p-i-n layers. However, two major differences exists. First, intrinsic region thickening is technologically more diffcult to accomplish and expenisve than fabricating a wide intrinsic regionin in the lateral structure. Second, in the lateral structure, light directly acts on the intrinsic region, whereas in the vertical structure, light must pass the substrate and TCO layers before the absorber layer is reached.

3.2.6 Effect of Surface Recombination in Lateral Structure

The surface of a Si solar cell also plays an important role in recombination. Hence, in Figure 3.21, I–V curves of the lateral cell (W = 13 μm) were simulated while considering the effect of both surface and bulk (herein only SRH is considered) recombinations. All the lateral cells attained similar J_{SC} values (Figure 3.21). However, V_{OC} diminishes from 659.46 mV to 610.58 mV because of the effect of bulk recombination (τ = 3.3 μs), and to 601.80 mV, and 487.45 mV, repectively, because of

surface recombination under the assumption of surface recombination velocities SRV = 100 and 1000 cm/s.

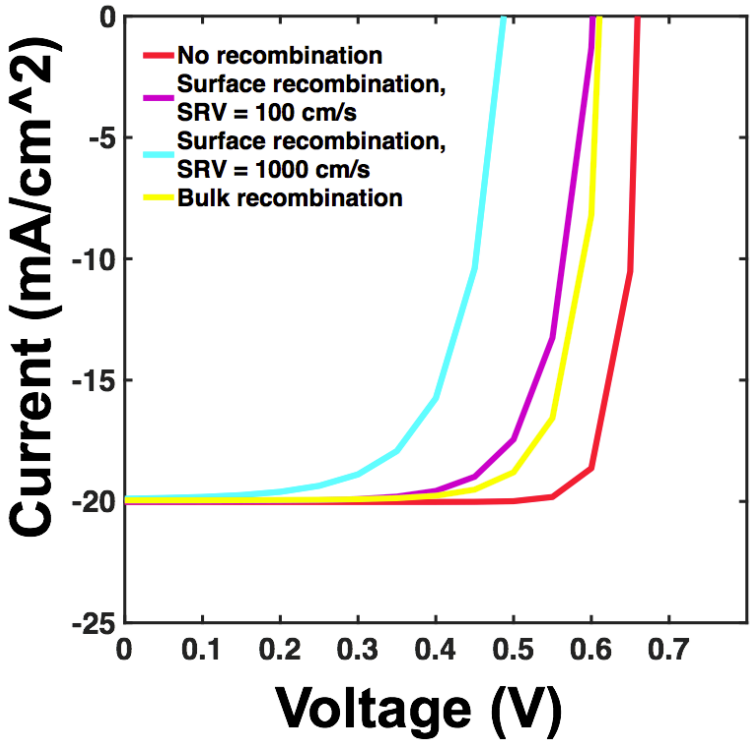

Figure 3.21 I–V curve of the lateral cell (W = 13 μm) in absence of recombination, considering bulk recombination (τ = 3.3 μs), ad surface recombination (SRV = 100 and 1000 cm/sec).

The simulation in Figure 3.21 illustrates the importance of passivation in the lateral p-i-n cell design. As the SRV increased from 100 to 1000 cm/s, the V_{OC} decreased by ~19%. This number shows that the requirements on the front surface passivation of this cell type are very high. For a lateral design, the surface area-to-volume ratio is so much larger than that of a vertical design, making the lateral device very

vulnerable to surface recombination. Most of the photo-generation occurs close to the front surface, where the carriers can easily be lost by recombining at a poorly passivated surface. Thus, a low front surface recombination (SRV) is one of the critical factors influencing the efficiency of the lateral cells.

As regards the advances in Si solar cell surface passivation techniques, the effec of surface recombination can be minimized [3.11, 3.12].

3.2.7. Effect of Contact Distance on Efficiency

In the following analysis, the focus was put on the distance d that carriers must travel from p/i or n/i junctions to reach contacts in Figure 3.22. this aspect is an important design parameter of the lateral structure. To investigate the effect of d on efficiency, a lateral cell was assumed with total width = 64 µm, W = 53 µm, $d_p = d_n = 5.5$ µm. Then d was increased from 0.5 µm to 5 µm by decreasing the width of contacts $d_{anode} = d_{cathode}$ from 5 µm to 0.5 µm. Considering practical issues, such as aligning resolution and cost, the minimum number of the d was assumed to be 0.5 µm.

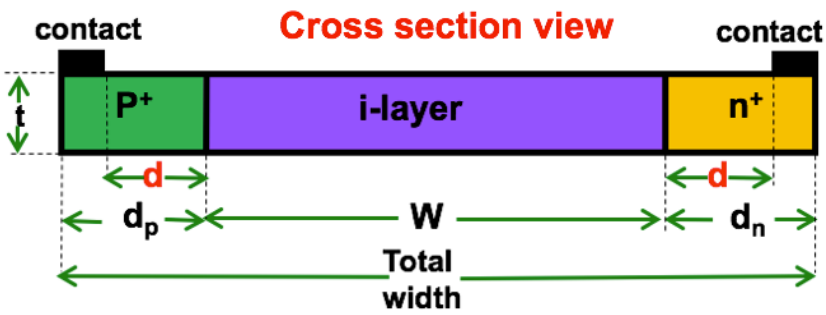

Figure 3.22 Cross section view of the lateral cell showing the distance between junctions and contacts (d).

Figure 3.23 shows the results of this simulation. It can be seen that the efficiency variation of the lateral cell with τ =10 μs and τ = 3.3 μs was rendered negligible by increasing d from 0.5 μm to 1 μm. However, their efficiency will be reduced by about 1% if the d is selected to be larger than 1 μm. For τ =100 μs, the behavior of efficiency variations versus d was similar to the previous cases. The only difference was the amount of efficiency reduction of 0.44%. Assuming the absence of recombination, it was noted the efficiency to increase by about 0.47% after d raised from 0.5 μm to 3 μm, and became saturated for d larger than 3 μm. Considering the effect of recombination, it was observed that by increasing the d, additional carriers were recombined before the contacts were reached and resulted in efficiency reduction. However, assuming the absence of recombination, it was noted that increasing the d up to 5 μm, opens additional opportunities for photon absorption.

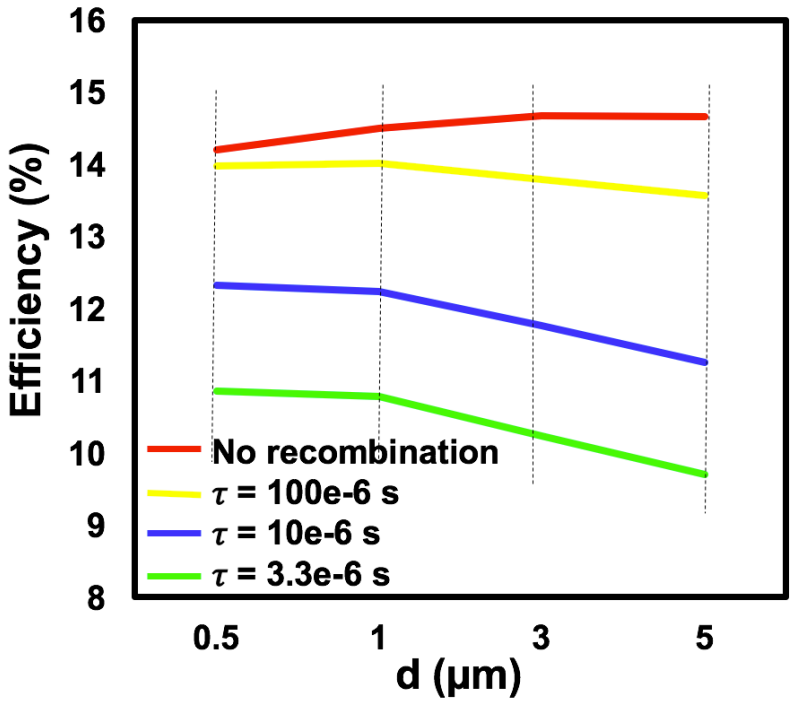

Figure 3.23 Efficiency of the lateral cell (W = 53 μm) as the function of the distance form p/i and n/i junctions to contacts, and τ as a parameter.

3.2.8 Effect of Temperature and Light Intensity

The size of lateral cell is small and its process needs photolithography, which causes higher fabrication cost compared to the vertical cells. However due to its high costs, the application of photolithography is usually allowed to the production of the small area concentrator solar cells. The cost of a concentrating PV system may be lower than a corresponding flat-plate PV system since only a small area of solar cells is needed [13]. In this section the effect of higher intensities of sun light was considered for simulation and the results are shown in Figure 3.24. The J_{SC} and V_{OC} increase under the effect of light intensity. A good

agreement between theory (Equation 3.10, where X is concentration of sunlight) and the results was observed.

$$V'_{OC} = \frac{nKT}{q} ln\left(\frac{X\, I_{SC}}{I_0}\right) = \frac{nKT}{q}\left[\ln\left(\frac{I_{SC}}{I_0}\right) + lnX\right] = V_{OC} + \frac{nKT}{q} lnX \quad (3.10)$$

From the equation above, a doubling of the light intensity (X=2) causes a 18 mV rise in V_{OC} .

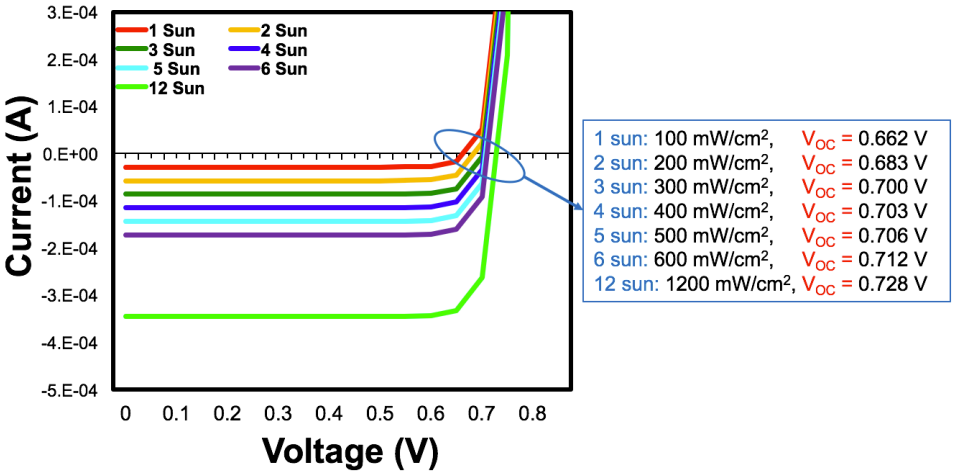

Figure 3.24 I-V curve of the lateral cell under the effect of different light intensities from one sun to 12 suns.

The behavior of the lateral cell depends on the ambient temperature as that of the conventional vertical cells. For Si, the theoretical estimation [3.14] gives a reduction in the open-circuit voltage V_{OC} of about 2.12 mV/K. The simulation results at various ambient temperature between 300 K and 400 K show that, while the short-circuit current remains nearly the same, V_{OC} decreases with reduction of ~2mV/K.

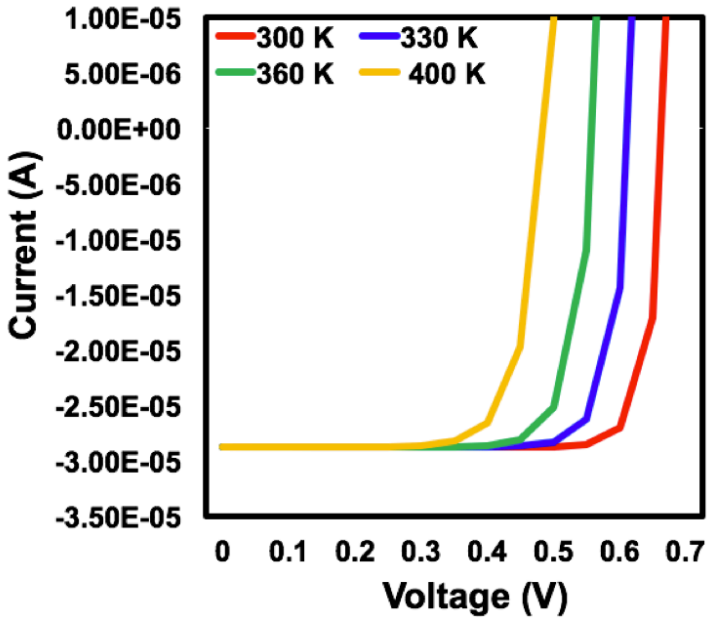

Figure 3.25 I-V curve of the lateral cell under the effect of different ambient temperature ranging from 300 K to 400 K.

3.3 Summary of Results and Comparison

Table 3.2 summarized the best simulation results obtained from the lateral p-i-n cell with different carrier's lifetime. The width of intrinsic region was set to 53 µm and the thickness of Si film was 3 µm. Moreover, the cell benefits from ARC and rear reflector. Obtained results in Table 3.2 confirms that the lateral structure can result in high efficiencies as long as the carrier lifetime is enough high.

Table 3.2 Summary of simulation results of the lateral p-in solar cell with

W = 53 μm.

Recombination	J_{SC} (mA/cm^2)	V_{OC} (mV)	FF (%)	η (%)
No recombination	24.18	709.86	84.7	14.54
τ =100 e-6 s	24.16	706.52	82.6	14.11
τ =10 e-6 s	23.93	671.95	77.01	12.38
τ =3.3 e-6 s	23.50	644.92	72.16	10.94

A summary of the comparison results of the narrow and relatively wide lateral cell with the vertical cell of the same area are presented in Table 3.3. In both cell types, the thickness (t) and length (L) were ~2 μm and 1cm, respectively. For the vertical cell, a 0.5 μm zinc oxide (ZnO) material was used as the TCO, and the thickness of the p- and n-type regions were set as respectively 0.03 and 0.1 μm, respectively. Results of Table 3.3 confirm the enhanced performance of the lateral structure specifically with wide intrinsic region. Notably, the efficiency of both lateral and vertical cells can be improved by considering light trapping or surface texturing, which are highly important for thin-film cells. For instance, such strategy can increase the efficiency of vertical p-i-n cells to above ~10% [3.15].

Table 3.3 Comparison of efficiency parameters between thin-film p-i-n Si solar cells of lateral and vertical type with total thickness of ~ 2 μm.

Cell Type	Width (μm)	J_{SC} (mA/cm^2)	V_{OC} (V)	Fil factor, FF (%)	η (%)
Lateral (Lateral Cell)	3	18.22	612.60	84.56	9.43
	15	20.66	660.07	84.74	11.55
Vertical (Conventional)	3	21.22	458.51	80.73	7.85
	15	21.28	456.12	80.10	7.77

3.4 Conclusion

Design, simulation and characterization results of lateral p-i-n solar cell is presented. The photovoltaic behavior of the lateral p-i-n diode for Si solar cell application was characterized. The structure holds major advantages as follows: direct light irradiation on the absorber layer, one side contact, possible use of the wide intrinsic layer, and applicability as bifacial solar cell. The considerable improvement in efficiency by ~1.7% confirmed the beneficial effect of intrinsic layer widening. The results showed excellent open-circuit voltage of 706.52 mV, short-circuit current of 24.16 mA/Cm^2, fill factor of 82.66%, and efficiency of 14.11% from a lateral cell of 3 μm thickness and 53 μm intrinsic layer. The design considerations that were outlined for highly efficient lateral p-i-n solar cells showed the potential of the laterally structured p-i-n Si solar cell to be a promising choice for photovoltaic devices.

Chapter 4. Fabrication of Lateral p-i-n Poly-Si Thin-film Solar cell by Ni Silicide-Induced Crystallization

In this chapter, fabrication of lateral thin-film poly-Si p-i-n solar cell is presented. A low-temperature, low-cost crystallization method; Ni silicide-induced crystallization was used to make thin-film poly-Si of the lateral cell. Two configurations were made; integration of isolated (Figure 4.1 (a)) and connected (Figure 4.1 (b)) lateral p-i-n cells.

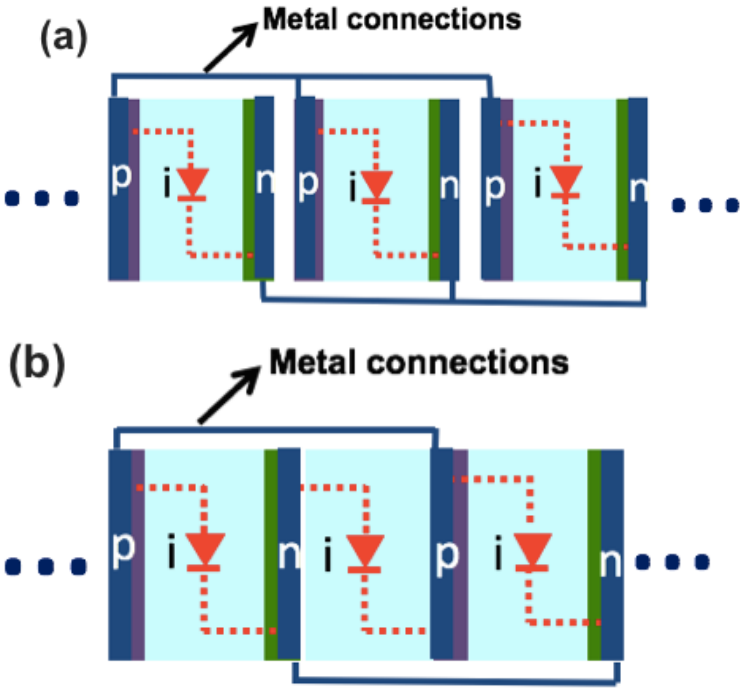

Figure 4.1 (a) Integration of isolated lateral p-i-n cells, and (b) Integration of connected lateral p-i-n cells.

4.1 Ni Silicide-Induced Crystallization(SIC)

The crystallization temperature of a-Si can be lowered by addition of some metals into a-Si and it is called metal induced crystallization (MIC). The MIC is induced by some metals such as Au [4.1], Al [4.2], Sb [4.3], and In [4.4], which form eutectics with Si, or metals such as Pd, Ti , and Ni [4.5, 4.6], which form silicide with Si. These metals have been added to a-Si to enhance the nucleation rate. Some of these cases were reported to be successful in lowering the crystallization temperature below 500°C. However, the MIC process has a serious drawback of undesirable incorporation of metal impurities into Si, so that it is not suitable for solar cell application. The quality of Si film is substantially important for efficiency of solar cell. Hence, it is of great significance to minimize the amount of metal incorporation into Si while a lower crystallization temperature is preferable. Thus, in this work silicide induced crystallization (SIC) was used, in which the Ni film is removed after Ni silicide formation.

In SIC process, after Ni sputtering (5 nm-thick) the sample is dipped in H_2So_4 solution at 110 ^{o}C for ~10 s to remove the Ni, and only the Ni silicide seeds, which are source of SIC, remains on the a-Si film (Ni reacts with a-Si to form $NiSi_2$).c-Si then nucleates at the interface between $NiSi_2$ and a-Si. Continued crystallization of c-Si is realized by migration of $NiSi_2$ into the a-Si film, leaving c-Si in its wake [4.7, 4.8].

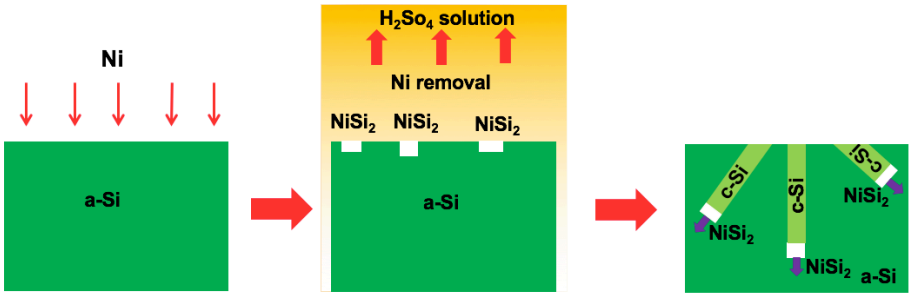

Figure 4.2 Ni silicide-induced crystallization; Ni deposition, Ni removal in H_2SO_4 solution, continued crystallization of a-Si.

4.2 Experimental Procedure

In this section the experimental procedure of lateral p-i-n poly-Si solar cell is presented. First, a 100-nm-thick Sio_2 was deposited on a glass substrate (Corning Eagle XG, 106 mm * 106 mm) through plasma enhanced chemical vapor deposition (PECVD) (Figure 4.3) at 350 ^{o}C for a buffer layer. Then, a 400-nm-thick intrinsic amorphous-silicon (a-Si) was deposited by PECVD at the same temperature. The sample was immersed into a piranha solution (H_2So_4:H_2O_2 = 3:1) to clean the Si surface and a BOE to strip the remaining native oxide. The Ni was deposited with 5 nm thick on the a-Si layer (Figure 4.4 (a)). After sputtering the sample is dipped in H_2So_4 at 110 ^{o}C for 10 s to remove the Ni, and only the Ni silicide seeds, which are source of SIC, remains on the a-Si film [4.9-4.11]. Afterward, the sample was annealed in a tube furnace at 550 ^{o}C in a vacuum for 4 h for crystallization (Figure 4.4 (b)). The poly-Si was then patterned using active mask and reactive ion etching (RIE). Afterward, the n and p type regions were defined and doped using PH_3 and B_2H_6, respectively, using an ion-mass doping system (IMD) (17 keV of accelerated voltage and 150 W of radio-

frequency (RF) power) (Figure 4.4 (c), (d)). It should be mentioned that due to the plasma in the IMD used for this experiments, it was not possible to use photo resist (PR) as the mask. Thus, oxide and metal layers were used for IMD mask. It unfortunately remained metal residual on Si film and reduced its quality. After defining the p and n-type regions, annealing was carried out at 550 ^{o}C in hydrogen ambient for 2 h for electrical activation. Finally, a 300-nm-thick $Mo_{0.9}W_{0.1}$ alloy for the metallization layer was deposited and patterned for contact or integration of the cells (Figure 4.4 (e)).

Figure 4.3 PECVD system used for a-Si deposition.

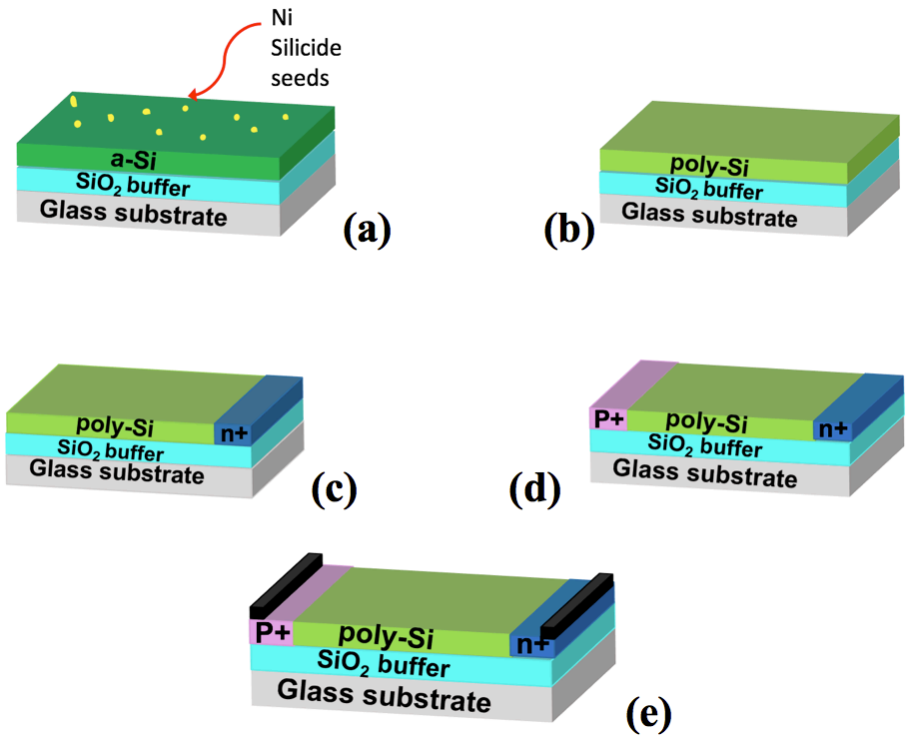

Figure 4.4 Fabrication process flow of lateral structured p-i-n poly-Si thin-film solar cell by low temperature Ni silicide-induced crystallization. (a) Ni sputter on a-Si film, Ni silicide seeds formation and annealing in vacuum ambient at 550 ^{o}C for crystallization, (b) poly-Si film, (c) and (d) p- and n-type region formation and doping, (e) electrical activation in H_2 ambient and metal contact formation.

All of the fabrication processes were carried out in a 1000-class clean room, and electrical characteristics were measured with Keithley 2636 and Agilent E5270B systems. A probe station with ring light source (white LEDs) were used with light intensity of less than 100 mW/cm^2 (Figure 4.5).

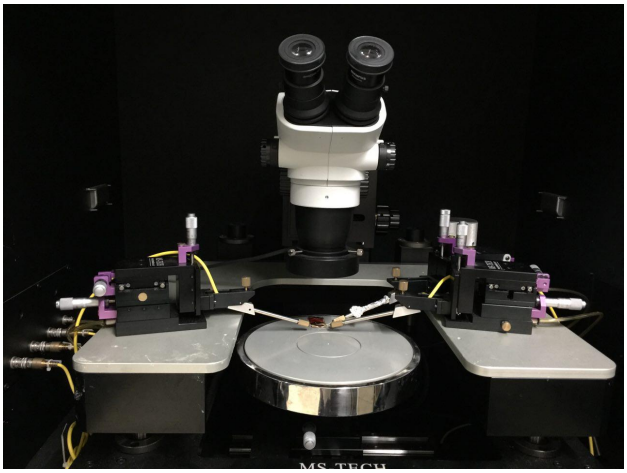

Figure 4.5 Probe station with ring light source (white LEDs) used for electrical measurement.

4.3 Experimental Results

4.3.1 I-V Characteristics of Isolated and Connected p-i-n Cells Under Dark and Light Illumination

The experimental results of lateral p-i-n poly-Si solar cell is presented in this section. In Figure 4.6 (a) and (b) I-V curves of isolated and connected lateral cells shown in Figure 4.1 (a) and (b), under dark and illumination is depicted. It was observed that isolated lateral cells generally show better I-V characteristic compared to the connected cells both under dark and illumination. Isolated cells show rectifying behavior with W up to 100 μm. However, the W of the connected cells should be less than 50 μm to ensure a reasonable rectifying behavior. The I-V curves of the isolated and connected cells showed 0.13 V and 0.15 V shifts under light illumination, respectively.

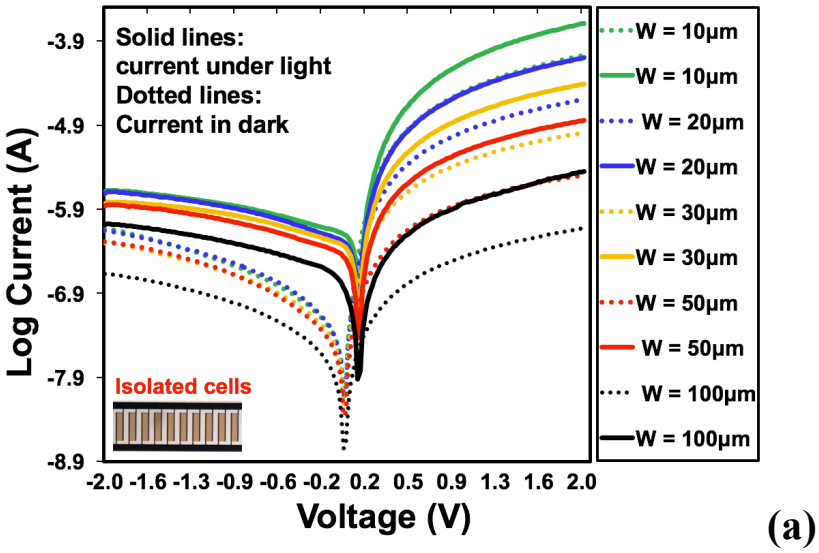

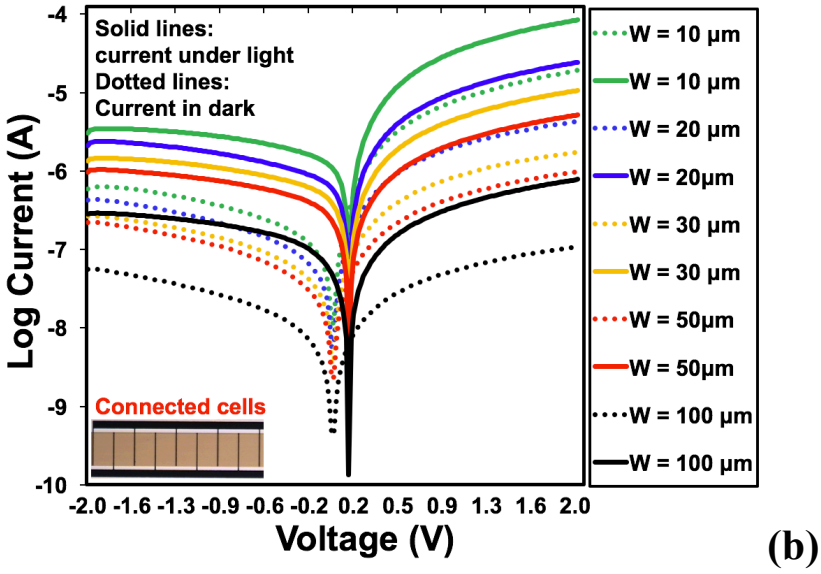

Figure 4.6 I-V characteristics of the fabricated lateral cells with various values of intrinsic region width under dark and light illuminated conditions (a) isolated cells, (b) connected cells.

4.3.2 The Best I-V Curve of Fabricated Isolated Lateral p-i-n Cell

Figure 4.7 shows the best I-V curve from the experimental results. A J_{SC} of 3.3 mA/cm^2 and a V_{OC} of 0.13 V in relatively thin 400-nm-thick cells. These results were measured from the isolated cells of the configuration shown in Figure 4.1(a) with a 200 µm long and 4 µm wide intrinsic region. The calculated J_{SC} value was normalized by the total area of intrinsic regions (effective illuminated active area). It should be noted that the results were obtained from cells without any optimization, such as light trapping, anti-reflection coating, glass texturing, and backside reflector. Thus, the optical path length of the cell is only thickness of the cell, which is ~400 nm. Indeed, by increasing the thickens of cell, using higher quality a-Si, and applying optical and electrical optimizations, better experimental results can be obtained.

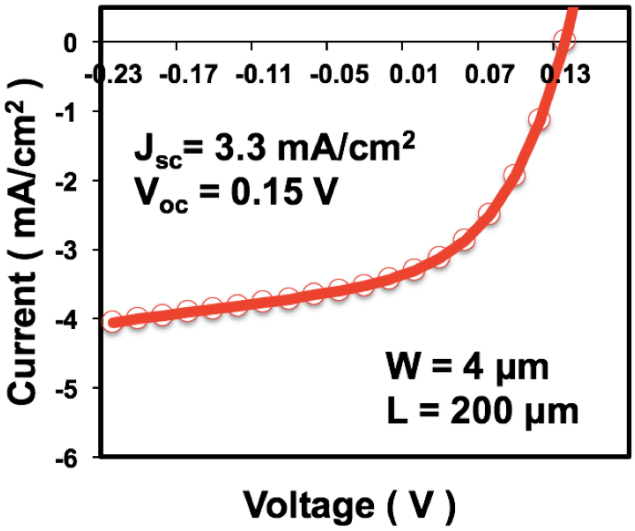

Figure 4.7 The best I-V curve, J_{SC} and V_{OC} of this work obtained from isolated cells with L = 200 µm and width W = 4 µm, and thickness of 400 nm.

4.3.3 Photo-Current Generation of Isolated and Connected p-i-n Cells as a Function of Intrinsic Region Width

Figure 4.8 shows the photo generated current of the isolated and connected cells for various intrinsic region widths. The former exhibited higher J_{SC} compared to the latter at the same values of W. In both lateral cells, J_{SC} reduced slowly by increasing W from 10 μm to 30 μm (cells with ultra-wide W). The decrease in photocurrent might be due to weakening of the built-in electric field in the intrinsic region. Thus, the drift length $L_{drift} = \tau \mu E_{bi}$ of the photo-generated carriers (where τ is the carrier lifetime, μ is the carrier mobility, and E_{bi} is the built-in electric field) needs to be sufficiently long to have a large photocurrent [4.12, 4.13]. Therefore, if the quality of the used material is not sufficiently high, lateral cells with ultra-wide W will not be highly efficient. In both lateral cells, V_{OC} had almost no change over W as could be expected.

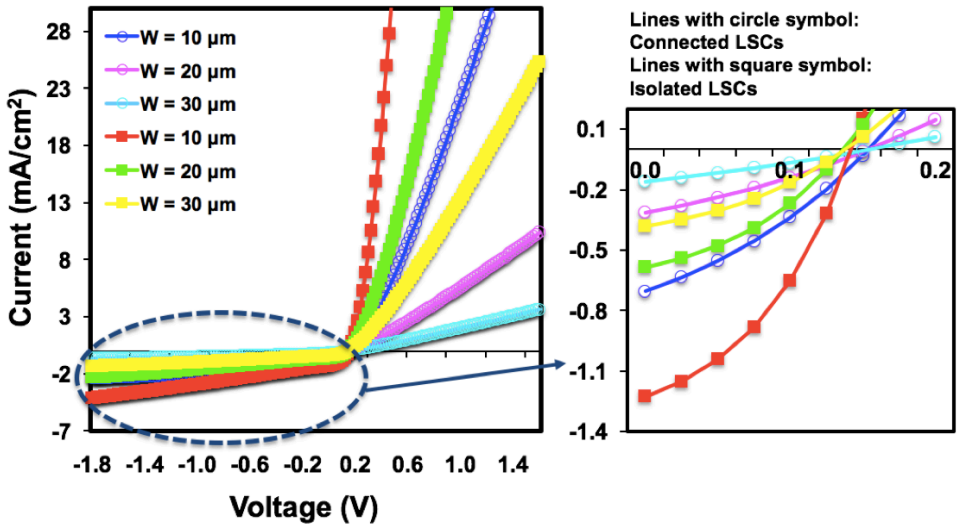

Figure 4.8 Photocurrent generation characteristics of isolated and connected cells under light illumination for different Ws. The intrinsic region length was fixed to L = 200 µm. Inset: magnification of the I-V curves.

4.3.4 I-V Characteristics of Comp-Shape Lateral p-i-n cell

Comp-shape pattern is one of possible structures for lateral solar cell. This structure is specifically suitable for low carrier life time materials, in which by reducing intrinsic region width (W_3 in Figure 4.9) and increasing number and length of fingers (p- and n-type regions covered by metal contact in Figure 4.9), the collection rate of carriers can be improved. Figure 4.10 illustrates I-V curve of a comp-shape lateral p-i-n cell with W_3 = 36 µm, W_1 = W_2 = 4 µm, W_4 = 0.5 µm, and thickness of 400 nm.

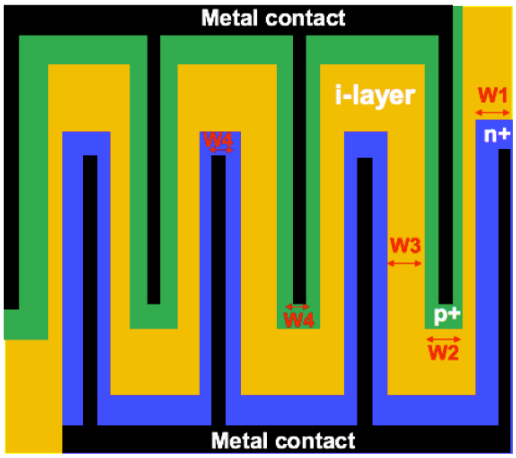

Figure 4.9 Comp-shape lateral p-i-n cell fabricated by Ni SIC method.

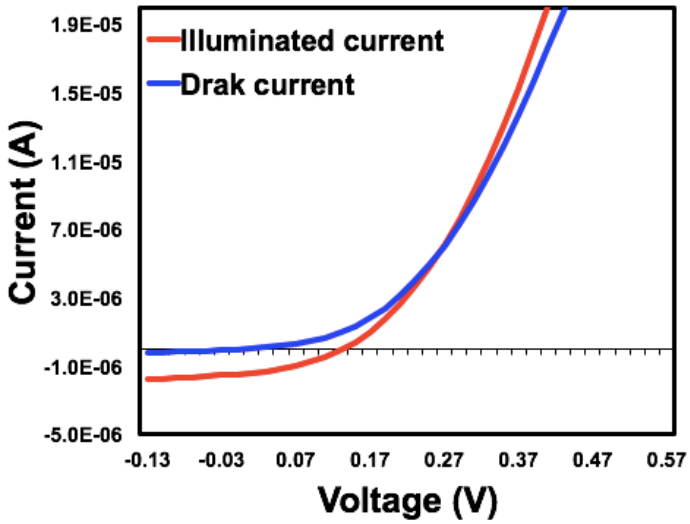

Figure 4.10 Dark and illuminated I-V curve of comp-shape lateral p-i-n cell with W_3 = 36 μm, W_1 = W_2 = 4 μm, W_4 = 0.5 μm, and thickness of 400 nm.

4.4 Summary of Pervious Works, Thin-film Poly-Si Solar Cell

The first attempt of practical implementation of lateral thin-film p-i-n

solar cell of this work is based on thin-film poly-Si. Thus, previous works of vertical structured poly-Si cells [4.14-4.17], [4.18, 4.19] were summarized in in Table 4.1. With regard to thin-film poly-Si fabrication cost including thermal budget (annealing time and temperature), substrate and equipment cost, SIC is cheap compared to others. However, SPC [4.14] is popular due to its technological simplicity. Laser [4.17], e-beam [4.18], and aluminum induced crystallization AIC methods are also desired due to large grain sizes.

Table 4.1 Poly-Si thin-film solar cells based on crystallization fabrication method.

Poly-Si Fabrication Method	**Grain Size (μm)**	**J_{SC} (mA/cm^2)**	**V_{OC} (mV)**	**η (%)**	**Source**
Solid phase crystallization (SPC)	1~3	29.5	492	10.5	Keevers et al. [14]
Seed layer approach (AIC)	10	20.7	534	8.0	Gordon et al. [15]
Direct crystallization growth	0.2	14.3	504	5.0	Carnel et al. [16]
Liquid phase crystallization (laser)	Up to 10000	24.2	557	8.4	Dore et al. [17]
Liquid phase crystallization (e-beam)	Up to 10000	13.5	582	4.3	Haschke et al. [18]
Ni Silicide-induced crystallization (SIC)	~20	3.3	150	-	This work

4.5 Conclusion

For the first time, a poly-Si thin-film lateral p-i-n solar cell was

fabricated and characterized. Two types of lateral cells: isolated and connected p-i-n cells were fabricated and compared. The isolated cells with W less than 100 μm, showed clear rectifying behavior. However, W of the connected cells must be less than 50 μm for the rectifying behavior. Generally, the isolated cells showed better I-V characteristics and J_{SC} than the connected cells at the same value of intrinsic region width. The V_{OC} of the isolated and connected cells were 0.13 V and 0.15 V, respectively. The best results obtained in this work without any optimization wee 3.3 mA/cm^2 of J_{SC} and 0.13 V of V_{OC} in 400-nm-thick isolated cells with a 200 μm long and 4 μm wide intrinsic region. Moreover, a comp-shape lateral cell was fabricated that is beneficial for materials with low carrier lifetime. Since thin-film lateral cells can be integrated using the semiconductor process, it can be expected to utilize the results obtained in this work for high voltage, low power integrated devices even though J_{SC} and V_{OC} are somewhat small.

Chapter 5. Summary and Conclusion

In this thesis, the lateral p-i-n diode for silicon solar cell application was suggested and studied. The focus was put on characterization of the lateral p-i-n diode for thin-film silicon solar cells. The performance of the suggested solar cell was investigated in details by simulation and experimental work.

In simulation chapter, efficiency parameters were calculated by considering the effect of different carrier lifetimes and recombination, as a function of intrinsic layer width, as well as the distance between p/i or n/i junctions to contacts, by simulation. From the results, optimum intrinsic region width was defined regarding carrier's lifetime of the cell. Obtained results showed that the distance between p/i or n/i junction to contacts should be kept below 1 μm in order to prevent efficiency reduction. Efficiency of the lateral cell increases by widening the intrinsic region.

The upper limits of W were defined regarding lifetime of carriers. For lateral cells with moderate and low carrier lifetime, maximum W is 13 μm. The upper limit of W increases to 53 μm for lateral cells with high carrier lifetime.

Moreover, in the simulation chapter, the effect of surface recombination on the performance of the lateral cell was evaluated by considering relatively low and relatively high surface recombination velocities (SRV). Simulation results of this work estimated a 19% decrease in V_{OC} by increasing SRV from 100 to 1000 cm/s for the lateral design. Thus, the requirements on the front surface passivation of the lateral cell type are very high, and surface recombination can be a

dominating performance limiting factor for lateral solar cell design. Excellent open-circuit voltage of 706.52 mV, short-circuit current of 24.16 mA/cm^2, and efficiency of 14.11% were achieved from simulated lateral cell with 3 μm thickness and 53 μm intrinsic layer width. The promising efficiency from simulation results confirm that the lateral structure is a potential powerful choice for solar cell industry and photosensitive energy source applications.

Moreover, feasibility of the lateral structure for solar cell application was demonstrated by experimental work. The performance of two configurations of lateral solar cells was investigated by experimental work. Lateral cells were successfully fabricated using polycrystalline-silicon (poly-Si) thin-film prepared by Ni silicide-induced crystallization (SIC) for the first time. I-V characteristics of two types of lateral cells, with isolated (p-i-n) cells and connected (p-i-n) cells were compared in dark and under illumination condition. The configuration with isolated cells showed clear rectifying behavior for a wider range of intrinsic region width compared to the connected cells.

At the same values of intrinsic region width, a higher short-circuit current was obtained from isolated cells than the connected cells. The short-circuit current of 3.3 mA/cm^2 and an open-circuit voltage of 0.13 V were obtained from a 400-nm-thick isolated cells. Regarding simulation results and the fact that no optimization was performed in the experimental work, it is expected to obtain higher efficiencies from fabrication, by means of optimizations such as surface texturing, light trapping, anti-reflection coating, and rear reflector.

Based on results of this work, higher efficiencies can be obtained from lateral structure compared to the vertical one.

However, the fabrication process of lateral cells is more complicated compared to the vertical cells and requires photolithography and masking steps. This results in higher manufacturing cost, and hence limits applications of the lateral solar cells.

Bibliography

CHAPTER 1

[1.1] United Nations, "World Population Prospects", http://esa.un.org/UNPP/, Retrieved **(2016).**

[1.2] http://solarcellcentral.com/solar_page.

[1.3] Cristina Archer, Mark Jacobson, "Evaluation of Global Wind Power", Stanford, Retrieved **(2016).**

[1.4] Food and Agriculture Organization of the United Nations, "Energy Conversion By Photosynthetic Organisms", Retrieved **(2016).**

[1.5] Energy Information Administration, "World Consumption of Primary Energy by Energy Type and Selected Country Groups, 1980-2004", Retrieved **(2016).**

[1.6] Energy Information Administration, "World Total Net Electricity Consumption, 1980-2005", Retrieved **(2016).**

[1.7] F. Granek, Ph.D. dissertation, Fraunhofer Institute for Solar energy, **(2009).**

[1.8] http://nsl.caltech.edu.

[1.9] State of the world 2009, http://www.worldwatch.org.

[1.10] NREL Compilation of Best Research Solar Cell Efficiencies. Data compiled by Lawrence Kazmerski, National Renewable Energy Laboratory (NREL). December **(2016).**

[1.11] S. Glunz, R. Preu, and D. Biro, *Comprehensive renewable energy 1,* 353 **(2012).**

[1.12] A. Shah, H. Schade, M. Vanecek, J. Meier, E. Vallat-Sauvain, N. Wyrsch, U. Kroll, C. Droz, and J. Bailat, Prog. *Photovolt:Res.Appl. 12,* 113 **(2004).**

[1.13] C. Becker, D. Amkreutz, T. Sontheimer, V. Preidel, D. Lockau, J. Haschke, L. Jogschies, C. Klimm, J. J. Merkel, P. Plocica, S. Steffens, and B. Rech, *Sol. Energ. Mat. Sol. Cells. 119*, 112 **(2013).**

[1.14] http://www.wealthdaily.com/report/solar-technology, **(2016).**

[1.15] K. L. Chopra, P. D. Paulson, and V. Dutta, Prog. *Photovolt:Res.Appl. 12,* 69 **(2004).**

[1.16] A. Aberle, *Thin Solid Films 517,* 4706 **(2009).**

[1.17] A. Shah, *Thin-film Silicon Solar Cell,* EPFL Press, Lausanne **(2010).**

[1.18] F. Meillaud, M. Boccard, G. Bugnon, M. Despeisse, S. Hanni, F. J. Haug, J. Persoz, J. W Schuttauf, M. Stuckelberger, and C. Balif, *Materials Today 18,* 378 **(2015).**

[1.19] K. Yamamoto, M. Yoshimi, Y. Tawada, Y. Okamoto, A. Nakajima, and S. Igari, *Appl. Phys. A. 69,* 179 **(1999).**

[1.20] M. A. Green, K. Emery, Y. Hishikawa, W. Warta, and E. D. Dunlop, *Prog. Photovolt:Res.Appl. 24,* 905 **(2016).**

[1.21] E. Singh, and H. S. Nalwa, *J. Nanosci. Nanotechnol. 15,* 6237 **(2015).**

CHAPTER 2

[2.1] http://en.wikipedia.org/wiki/Theory_of_solar_cell.

[2.2] http://www.pveducation.org/pvcdrom/short-circuit-current.

[2.3] http://www.pveducation.org/pvcdrom/open-circuit-voltage.

[2.4] http://www.pveducation.org/pvcdrom/fill-factor-0.

[2.5] A. Shah, Thin-film Silicon Solar Cell, EPFL Press, Lausanne **(2010).**

[2.6] X. Deng, and E. A. Schiff, Amorphous Silicon Based Solar Cells. In *Handbook of Photovoltaic Science and Engineering,* Luque A, Hegedus S (eds). John Wiley and Sons: Chichester, UK **(2003).**

[2.7] H. Peelaers, E. Kioupakis, and C. G. Van de Walle, *Appl. Phys. Lett. 100,* 011914 **(2012).**

[2.8] A. B. C. Lopez, A. M. Vega, and A. L. Lopez, Next Generation of Photovoltaics: New Concepts, Springer, Berlin **(2012).**

[2.9] F. Meillaud, A. Billet, C. Battaglia, M. Boccard, G. Bugnon, P. Cuony, M. Charriere, M. Despeisse, L. Ding, J. Escarre-Palou, S. Hanni, L. Lofgren, S. Nicolay, G. Parascandolo, M. E. Stuckelberger, and C. Ballif, *IEEE J. Photovolt. 2,* 236 **(2012).**

[2.10] A. Shah, H. Schade, M. Vanecek, J. Meier, E. Vallat-Sauvain, N. Wyrsch, U. Kroll, C. Droz, and J. Bailat, *Prog. Photovolt:Res.Appl. 12,* 113 **(2004).**

[2.11] M. Lammert, and R. Schwartz, *IEEE Trans. Electron Devices 24,* 337 **(1997).**

[2.12] M. Kim, J. H. Park, J. H. Kim, J. H. Sung, S. B. Jo, M. H. Jo, and K. Cho, *Adv. Energy Mater. 5,* 1 **(2015).**

[2.13] H. Ohtsuka, M. Sakamoto, K. Tsutsui, and Y. Yazawa, *Prog. Photovolt:Res.Appl. 8,* 385 **(2000).**

CHAPTER 3

[3.1] www.lumerical.com.

[3.2] D. Meier, D. Schroder, *IEEE Trans. Electron Devices* 31, 647 **(1984).**

[3.3] D. Schroder, D. Meier, *IEEE Trans. Electron Devices* 31, 637 **(1984).**

[3.4] A. Shah, *Thin-film Silicon Solar Cell,* EPFL Press, Lausanne **(2010).**

[3.5] R. N. Hall, *Phys. Rev.* 87, 387 **(1952).**

[3.6] J . Dziewior and W . Schmid, *Appl. Phys. Lett. 31,* 346 **(1977).**

[3.7] K.G. Svantesson and N. G. Nilsson, *J. Phys. C 12,* 5111 **(1979).**

[3.8] A. Haug, *Solid State Communications 25,* 477 **(1978).**

[3.9] R. A. Sinton, and R. M. Swanson, *IEEE Trans. Electron Dev. 34,* 6 **(1987).**

[3.10] A. V. Palankovski, S. Selberherr, and G. Golan, *Silicon* 7, 283

(2015).

[3.11] M. Rahman, S. Khan, *Materials for Renewable and Sustainable Energy. 1,* 1 **(2012).**

[3.12] J. Schmidt, A. Merkle, R. Brendel, B. Hoex, M. C. M. Van de Sanden, and W. M.Kessels, *Prog. Photovolt: Res. Appl. 15,* 659 **(2007).**

[3.13] F. Granek, Ph.D. dissertation, Fraunhofer Institute for Solar energy, **(2009).**

[3.14] A. R. Burgers, *Prog. Photovolt: Res. Appl.* 7, 457 **(1999).**

[3.15] M. A. Green, K. Emery, Y. Hishikawa, W. Warta, and E. D. Dunlop, *Prog. Photovolt:Res.Appl*. 24, 905 **(2016).**

CHAPTER 4

[4.1] G. Ottaviani, D. Sigurd, V. Marrello, J. W. Mayer, and J. O. MeCaldin, *J. Appl. Phys.45,* 1730 **(2003).**

[4.2] L. Hultman, A. Robertson, H. T. G. Hentzell, and I. Engstron, *J. Appl. Phys. 62,* 3647 **(1987).**

[4.3] S. F. Gong, H. T. G. Hentzell, A. E. Robertsson, L. Hultman, S. E. Hornstrom, and G. Radnoczi, *J. Appl. Phys* .62, 3726 **(1987).**

[4.4] E. Nygren, A. P. Pogany, K. T. Short, J. S. Williams, R. G. Elliman, and J. M. Poate, *Appl. Phys. Lett. 52,* 439 **(1988).**

[4.5] R. J. Nemanichi, C. C. Tsai, M. J. Thompson, and T. W. Sigmon, *J. Vac. Sci. Technol. 19,* 685 **(1981).**

[4.6] R. J. Nemanici, R. T. Fulks, B. L. Stafford, and H. A. Vanderpals, *J. Vac. Sci. Technol. A3,* 938 **(1985).**

[4.7] S. K. Joo*, Electronic Materials Letters 1,* 7 **(2005).**

[4.8] Z. Wang, L. P. H. Jeurgens, E. J. Mittemeijer, *Metal-induced Crystallization: Fundamentals and Applications,* CRC Press, NW **(20015).**

[4.9] C. W. Byun, S. W. Son, Y. W. Lee, H. M. Kang, S. A. Park, W. C. Lim, T. Li, and S. K. Joo, *J. Electrochem. Soc. 159,* J115 **(2012).**

[4.10] S. J. Yun, Y. W. Lee, S. W. Son, C. W. Byun, and S. K. Joo, "Leakage current behavior of bottom gate poly thin-film transistor fabricated by copper damascene process," J. Nanosci. Nanotechnol **13**, 7155 – 7157 (2013).

[4.11] C. W. Byun, S. W. Son, Y. W. Lee, H. M. Kang, S. A. Park, W. C. Lim, T. Li, and S. K. Joo, "High performance poly-Si thin-film transistors fabricated by novel and simple crystallization method using Ni-silicide seeds," J. Electrochem. Soc. **158**, J354–J358 (2011).

[4.12] J. Nelson, J. Kirkpatrick, and P. Ravirajan, *Phys. Rev. B 69,* 035337 **(2004).**

[4.13] J. Haschke, L. Jogschies, D. Amkreutz, L. Korte, and B. Rech, *Sol. Energ. Mat. Sol. Cells. 115,* 7 **(2013).**

[4.14] T. Matsuyama, N. Terada, T. Baba, T. Sawada, S. Tsuge, K. Wakisaka, and S. Tsuda, *J. Non-Cryst. Solids 198,* 940 **(1996).**

[4.15] I. Gordon, L. Carnel, D. Van Getel, G. Beaucarne, and J.

Poortmans, *Prog. Photovolt: Res. Appl 15,* 575 **(2007).**

[4.16] L. Carnel, I. Gordon, D. Van Gestel, G. Beaucane, and J. Poortmans, *J. Appl. Phys 100,* 063702 **(2006).**

[4.17] J. Dore, R. Evans, U. Schubert, B. D. Eggleston, D. Ong, K. Kim, J. Huang, O. Kunz, M. Keevers, R. Egan, S. Varlamov, and M. A. Green, "Thin-film polycrystalline silicon solar cells formed by diode laser crystallization", *Prog. Photovolt: Res. Appl 21,* 1377 **(2013).**

[4.18] J. Haschke, L. Jogschies, D. Amkreutz, L. Korte, and B. Rech, *Sol. Energ. Mat. Sol. Cells. 115,* 7 **(2013).**

국문초록

실리콘 태양전지를 위한 측면 p-i-n 다이오드

조레
서울대학교 공과대학 재료공학부

본 학위논문은 횡방향(lateral) p-i-n 다이오드 구조를 실리콘 태양전지에 적용하기 위한 방법을 다룬다. 횡방향 다이오드 구조를 사용할 경우 광흡수층이 단방향 접촉만을 가지므로 태양광이 광흡수층에 직접 조사될 수 있을 뿐만 아니라 넓은 진성(intrinsic) 영역을 가질 수 있다는 장점에 주목하여, 실리콘 박막전지에 이러한 횡방향 p-i-n 다이오드 구조를 적용 및 분석하기 위한 연구를 최초로 수행하였다.

전하운반체의 수명시간(lifetime) 및 재결합(recombination) 수준의 변화를 고려하여, 횡방향 실리콘 박막태양전지의 성능지표를 진성영역의 너비에 따른 함수로 혹은 p/i 또는 n/i 접합과 금속전극 사이의 거리에 따라 계산하기 위한 시뮬레이션 분석을 진행하였다. 시뮬레이션 결과를 통하여 전하운반체의 수명시간에 따른 진성영역 너비의 최적치를 계산하였다. 또한, 효율 저하를 방지하기 위해서는 p/i 혹은 n/i 접합과 금속전극의 간격이 1 μm 이하로 유지되어야 함을 확인하였다.

이에 더하여, 시뮬레이션 분석에서는 표면 재결합 속도(surface recombination velocity; SRV)가 상대적으로 느린 경우 혹은 빠른 경우를 가정하여 SRV가 횡방향 실리콘 박막태양전지의 성능에 미치는 영향을 분석하였다. 시뮬레이션 결과 SRV가 100 cm/s to 1000 cm/s로 높아짐에 따라 개방회로전압이 약 19% 감소하는 것을 확인하였고, 따라서

기존의 종방향(vertical) 구조와 비교할 때 횡방향 구조에서 전면부의 표면결함 부동화(passivation) 공정이 중요하다는 점을 규명하였다. 횡방향 p-i-n 구조를 적용한 실리콘 박막태양전지(셀 두께 3 μm, 진성영역 너비 53 μm)에 대한 특성 시뮬레이션 결과 706.52 mV의 개방회로전압, 24.16 mA cm^{-2} 의 단락회로전류, 82.66%의 필 팩터(fill factor; FF)를 얻어, 14.11%의 광전변환효율을 얻을 수 있을 것으로 예측되었다.

이러한 시뮬레이션 분석과 병행하여, 종방향 다이오드 구조를 적용한 서로 다른 두 가지 종류의 태양전지 구조에 대한 실험 분석을 진행하였다. 니켈실리사이드를 사용한 실리사이드 유도 결정화 (silicide-induced crystallization; SIC)법을 통해 다결정 실리콘 박막을 합성하는 데 최초로 성공하였다. 고립형(isolated) p-i-n 구조 및 연결형(connected) p-i-n 두 가지 형태의 종방향 셀에서 암실환경 및 광조사 환경의 전류-전압 특성을 비교하였다. 연결형 구조와 비교할 때 고립형 구조의 경우 보다 넓은 진성영역 너비에서 유래하는 뚜렷한 정류특성을 보였다. 진성영역 너비를 동일하게 유지한 경우 연결형 구조에 비하여 고립형 구조에서 보다 높은 단락회로전류를 얻었다. 구체적으로, 400 nm 두께로 제작된 고립형 셀에서 3.3 mA cm^{-2} 의 단락회로전류 및 0.13 V 의 개방회로전압이 확인되었다. 실험 분석에서 어떠한 공정 최적화 과정도 진행되지 않은 점 및 시뮬레이션 결과에 의한 예측으로부터, 표면 텍스쳐링(surface texturing)과 광포획(light trapping), 무반사코팅(anti-reflective coating) 및 후면반사막(rear reflector) 등 셀 구성요소의 최적화를 통하여 보다 높은 효율을 얻을 수 있을 것으로 기대된다.

본 연구 결과는 비록 현재로서는 복잡한 제조공정 및 그로 인한 고비용을 필요로 하지만, 횡방향 p-i-n 구조가 고효율

실리콘 태양전지 구현을 위하여 가능한 접근임을 확인하였다.

주요어: 태양 전지, p-i-n 다이오드, 횡방향(lateral) 태양 전지, 폴리 실리콘, 실리사이드 유도 결정화, 시뮬레이션

학번: 2014-30857